CASL-U-2015-0015-000

Modeling Integral Fuel Burnable Absorbers Using the Method of Characteristics

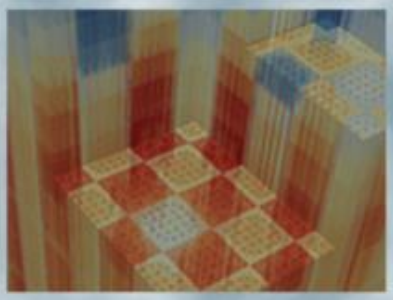

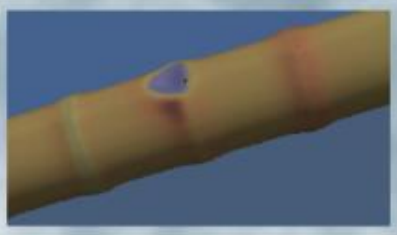

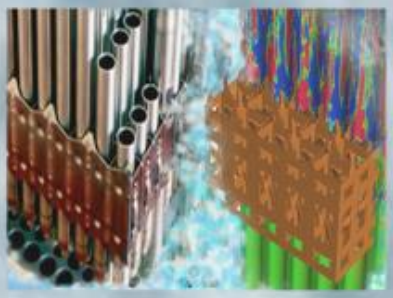

Erik Daniel Walker
University of Tennessee, Knoxville

December 1, 2014

U.S. DEPARTMENT OF ENERGY | Nuclear Energy

CASL-U-2015-0015-000

University of Tennessee, Knoxville
Trace: Tennessee Research and Creative Exchange

Masters Theses | Graduate School

12-2014

Modeling Integral Fuel Burnable Absorbers Using the Method of Characteristics

Erik Daniel Walker
University of Tennessee - Knoxville, ewalk@vols.utk.edu

Recommended Citation
Walker, Erik Daniel, "Modeling Integral Fuel Burnable Absorbers Using the Method of Characteristics. " Master's Thesis, University of Tennessee, 2014.
http://trace.tennessee.edu/utk_gradthes/3191

This Thesis is brought to you for free and open access by the Graduate School at Trace: Tennessee Research and Creative Exchange. It has been accepted for inclusion in Masters Theses by an authorized administrator of Trace: Tennessee Research and Creative Exchange. For more information, please contact trace@utk.edu.

To the Graduate Council:

I am submitting herewith a thesis written by Erik Daniel Walker entitled "Modeling Integral Fuel Burnable Absorbers Using the Method of Characteristics." I have examined the final electronic copy of this thesis for form and content and recommend that it be accepted in partial fulfillment of the requirements for the degree of Master of Science, with a major in Nuclear Engineering.

Jess C. Gehin, Major Professor

We have read this thesis and recommend its acceptance:

G. Ivan Maldonaldo, Ronald E. Pevey, Lawrence W. Townsend

Accepted for the Council:
Carolyn R. Hodges

Vice Provost and Dean of the Graduate School

(Original signatures are on file with official student records.)

Modeling Integral Fuel Burnable Absorbers Using the Method of Characteristics

A Thesis Presented for the
Master of Science
Degree
The University of Tennessee, Knoxville

Erik Daniel Walker
December 2014

CASL-U-2015-0015-000

Copyright © 2014 by Erik Daniel Walker
All rights reserved.

CASL-U-2015-0015-000

This thesis is dedicated to my family and girlfriend for their unending support.

CASL-U-2015-0015-000

Acknowledgements

I wish to show my appreciation to my advisor, Dr. Jess Gehin, for his guidance, mentorship, and for giving me the opportunity to pursue higher education while working at ORNL. I want to also thank Dr. Lee Riedinger and the University of Tennessee Bredesen Center for Interdisciplinary Research and Graduate Education for providing funding for this work. I would like to acknowledge my thesis committee: Dr. Ivan Maldonado, Dr. Ronald Pevey, and Dr. Lawrence Townsend for their help with the completion of this thesis. Finally, I wish to thank all those who have helped me throughout this process, especially Andrew Godfrey, Dr. Ben Collins, and Dr. Matt Jessee for taking time out of their busy schedules to help me and to answer my never ending questions.

This research was supported by the Consortium for Advanced Simulation of Light Water Reactors (www.casl.gov), an Energy Innovation Hub (http://www.energy.gov/hubs) for Modeling and Simulation of Nuclear Reactors under U.S. Department of Energy Contract No. DE-AC05-00OR22725. This research used resources of the Oak Ridge Leadership Computing Facility at the Oak Ridge National Laboratory, which is supported by the Office of Science of the U.S. Department of Energy under Contract No. DE-AC05-00OR22725.

Abstract

Modern core designs that utilize Westinghouse fuel technology employ the use of Integral Fuel Burnable Absorbers (IFBA) that consists of very thin coatings of boron absorber material on the fuel pellets. While IFBA has proven to be an effective burnable absorber, it does present a neutronics modeling challenge. The difficulty of modeling IFBA using the Method of Characteristics (MOC) transport method is well known, and arises from the fact that IFBA is a very small, but also very important, region in nuclear fuel. Experience in modeling IFBA at the pin cell and single assembly lattice level requires a decrease in the MOC ray spacing leading to substantial increases in computation times. This would represent a significant computational challenge for modeling cores containing IFBA with new methods that use full 2D planar MOC calculations, such as that being developed for the Consortium for Advanced Simulation of Light Water Reactors (CASL) Virtual Environment for Reactor Applications (VERA).

An investigation of modeling IFBA using MOC was performed to address concerns about accurately modeling IFBA. The accuracy of modeling IFBA using MOC at various ray spacings was examined for different problems using the Michigan Parallel Analysis based on Characteristic Tracing (MPACT) MOC code. For a single 2D IFBA pin cell, there is an extreme dependence on ray spacing for accurate results. This dependence was reduced when a 2D assembly containing IFBA was modeled. An AP1000® full core 2D midplane was modeled, and the effect of ray spacing on accuracy was much less drastic. The accuracy assessments were based both on the eigenvalue and pin power differences when compared to a high fidelity Monte Carlo calculation of the same model. The effect of volume weighting the IFBA material and then smearing it into neighboring regions was examined, and was found to be a less accurate method for modeling IFBA. Depletion cases of the AP1000 model were run to determine the impact of IFBA on the life of the core. It was found that standard ray spacing and step sizes are sufficient for accurately performing full core depletion calculations, but special care is needed for problems of smaller scale.

Table of Contents

1. Introduction and Background 1
1.1 Integral Fuel Burnable Absorbers 2
1.2 Open Literature Search 3
1.3 Research Goals 4
1.4 MPACT 5
1.4.1 Multigroup Approximation 6
1.4.2 The Discrete Ordinates Approximation 7
1.4.3 Spatial Discretization 8
1.4.4 Segment Length 9
2. Models 10
2.1 2D IFBA Pin Cell 10
2.2 2D IFBA Lattice 11
2.3 2D Full Core AP1000 Midplane 11
2.4 Extreme Case 16
2.5 Volume Weighted Smearing 16
2.6 Reference Solutions 17
3. Results and Discussion 18
3.1 2D IFBA Pin Cell 18
3.2 2D IFBA Lattice 19
3.3 2D Full Core AP1000 Midplane 22
3.4 Extreme Case 24
3.5 Volume Weighted Smearing 25
3.6 Non-Volume Weighted Segment Lengths 27
3.7 Depletion 31
3.8 Run Time 33
4. Conclusions 35
References 36
Appendices 38
Appendix A – 2D IFBA Pin Cell VERA Input 39
Appendix B – 2D IFBA Lattice VERA Input 41

Appendix C – Full Core AP1000 2D Midplane Input 44
Vita..... 50

List of Tables

Table 1: 2D pin cell input specifications 10
Table 2: 2D lattice additional input specifications 11
Table 3: AP1000 input specifications 12
Table 4. AP1000 fuel enrichments by region.....13
Table 5: WABA burnable poison specification 14
Table 6: Summary of run times for all depletion cases.....33

List of Figures

Figure 1. Schematic of a typical PWR [2] 1
Figure 2. Characteristic tracks intersecting the IFBA layer [4] 3
Figure 3. Macro-band approach [4] 4
Figure 4. 2D representation of a pin cell [13] 10
Figure 5. 2D IFBA quarter assembly geometry [13] 11
Figure 6. AP1000 assembly map in quarter symmetry 12
Figure 7. Assembly fuel enrichment configuration for regions 4 and 5 in quarter symmetry 13
Figure 8. WABA geometry in 2D [13] 14
Figure 9. 68 (left), 88 (middle), and 124 (right) IFBA configurations in octant symmetry 15
Figure 10. 4 (left), 8 (middle), 12 (right) WABA configurations in octant symmetry 15
Figure 11. IFBA and WABA burnable absorber placement in AP1000 quarter core 15
Figure 12. IFBA and WABA burnable absorber placement in extreme case in quarter symmetry 16
Figure 13. k-eff differences of CASL VERA Core Physics Benchmark Problem 1E 18
Figure 14. Run time of CASL VERA Core Physics Benchmark Problem 1E 19
Figure 15. k-eff differences of CASL VERA Core Physics Benchmark Problem 2M at various ray spacings compared to CE-KENO 20
Figure 16. Pin power differences of CASL VERA Core Physics Benchmark Problem 2M at various ray spacings compared to CE-KENO 20
Figure 17. Pin power difference map of CASL VERA Core Physics Benchmark Problem 2M in quarter symmetry between MPACT and CE-KENO using the default ray spacing 21
Figure 18. Run time of CASL VERA Core Physics Benchmark Problem 2M 21
Figure 19. k-eff differences of AP1000 Full Core 2D Plane at various 22
Figure 20. Pin power differences of AP1000 Full Core 2D Plane at various 23
Figure 21. Run time of AP1000 Full Core 2D Plane at various ray spacings 23
Figure 22. Pin power difference map of AP1000 Full Core 2D Plane in quarter symmetry between MPACT and CE-KENO using the default ray spacing 24
Figure 23. k-eff differences of AP1000 Full Core 2D Plane with every other assembly made entirely of IFBA at various ray spacings compared to 0.001 cm ray spacing 25
Figure 24. k-eff differences of AP1000 Full Core 2D Plane with smeared IFBA regions at various ray spacings compared to CE-KENO 26
Figure 25. Pin power RMS differences of AP1000 Full Core 2D Plane with smeared IFBA regions at various ray spacings compared to CE-KENO 26
Figure 26. Maximum pin power differences of AP1000 Full Core 2D Plane with smeared IFBA regions at various ray spacings compared to CE-KENO 27
Figure 27. Segment length volume weighting factors for 2D single pin cell 28
Figure 28. Segment length volume weighting factors for full core AP1000 2D midplane 28
Figure 29. Eigenvalue differences for 2D pin cell compared to CE-KENO for both volume weighting and not volume weighting cases 29

Figure 30. Eigenvalue differences for full core AP1000 2D midplane compared to CE-KENO for both volume weighting and not volume weighting cases 30
Figure 31. RMS pin power differences for full core AP1000 2D midplane compared to CE-KENO for both volume weighting and not volume weighting cases 30
Figure 32. Maximum pin power differences for full core AP1000 2D midplane compared to CE-KENO for both volume weighting and not volume weighting cases 31
Figure 33. Boron concentration differences of AP1000 Full Core 2D Plane at various ray spacings compared to benchmark case 32
Figure 34. Boron concentration differences of AP1000 Full Core 2D Plane with different step sizes compared to benchmark case 33
Figure 35. Comparison of boron concentrations between the benchmark and standard cases ... 34

Abbreviations

2D	Two-Dimensional
BOL	Beginning of Life
CASL	Consortium for Advanced Simulation of Light Water Reactors
CE	Continuous Energy
DOE	U.S. Department of Energy
HZP	Hot Zero Power
IFBA	Integral Fuel Burnable Absorbers
kWh	kilowatt hours
MOC	Method of Characteristics
MPACT	Michigan Parallel Analysis based on Characteristic Tracing
PCM	Per Cent Mille
PWR	Pressurized Water Reactor
RMS	Root Mean Square
VERA	Virtual Environment for Reactor Applications
WABA	Wet Annular Burnable Absorbers

1. Introduction and Background

The United States Energy Information Administration projects the total electricity demand in the U.S. to increase by 29% from 3,826 billion kilowatt-hours (kWh) in 2012 to 4,954 billion kWh in 2040 [1]. With this increase in electricity demand, nuclear power will be an important carbon-free base load option for meeting this projection. Nuclear power plants generate power by converting the thermal energy released from the fission of the nuclear fuel within the reactor into electricity. There are currently 100 commercial nuclear reactors licensed to generate power in the United States. Roughly two thirds of these, 65, are pressurized water reactors (PWR) [2]. In PWRs, the primary coolant system, which is roughly 600 °F, is kept in a liquid state by pressurizing the system. This thermal energy is then transferred to a secondary coolant loop through a heat exchanger called a steam generator. The secondary coolant is allowed to turn to steam, which is then directed into a turbine generator that produces electricity. A schematic of the layout of a typical PWR is shown in Figure 1.

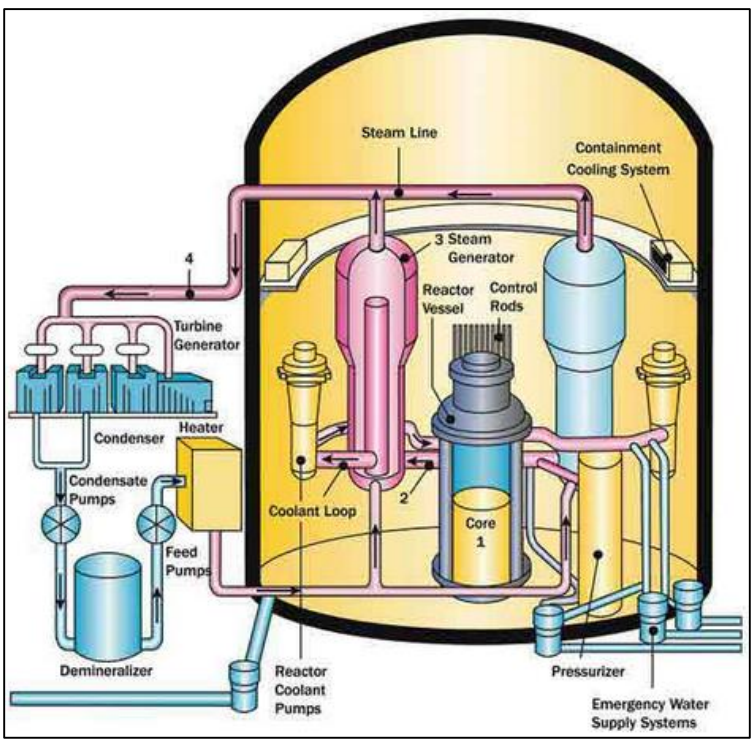

Figure 1. Schematic of a typical PWR *[2]*

Modeling and simulation are becoming increasingly valuable tools used to accurately predict reactor performance and improve safety throughout the life of the plant. The Consortium for Advanced Simulation of Light Water Reactors (CASL) is a U.S. Department of Energy (DOE) Energy Innovation Hub tasked with developing advanced modeling and simulation capabilities

for the nuclear industry. This suite of capabilities is known as the Virtual Environment for Reactor Applications (VERA) and includes chemistry, neutronics, thermal-hydraulics, and thermo-mechanics components. One of the neutron transport codes developed in VERA is Michigan Parallel Analysis based on Characteristic Tracing (MPACT). MPACT solves the characteristic form of the Boltzmann transport equation using the Method of Characteristics (MOC), first proposed by Askew in 1972 [3]. MOC is a general mathematical technique for solving first-order partial differential equations and is an attractive neutron transport technique because it avoids some of the drawbacks associated with other methods; it is relatively simple to implement while computation time and memory requirements scale linearly with the spatial and angular detail of the problem [4]. MOC is implemented by solving the characteristic form of the Boltzmann transport equation along discrete tracks, oriented at different angles that are traced over the explicit problem geometry. Every unique angle is given a weight and the average angular flux along each track is calculated. The solutions from each track are combined and produce a very accurate description of the flux distribution throughout the problem. However, MOC has trouble accurately modeling very small regions if the ray or angular discretization is larger than the region thickness. This becomes a significant problem when the small region being modeled is also highly absorbing.

1.1 Integral Fuel Burnable Absorbers

While there are many different types of burnable absorbers, an Integral Fuel Burnable Absorber (IFBA) is a Westinghouse product and is extensively used in Westinghouse PWRs today. IFBA is a thin coating of ZrB_2 that is deposited on the outside of fuel pellets in order to reduce power peaking and to suppress excess reactivity near the beginning of the fuel cycle. The layer is typically on the order of 0.001 cm thick. The boron in the IFBA layer is a strong neutron absorber and therefore decreases the neutron population in the area of the IFBA rod. The IFBA design is such that the B^{10} will completely deplete in the first fuel cycle, eliminating any residual reactivity penalty. Another advantage is that it does not displace any fuel in the core. IFBA leads to improved core design efficiency that saves on fuel costs. Therefore, IFBA is a critical part of reactor designs and as a result, it is imperative that it can be modeled accurately.

Because IFBA is so highly absorbing, the MOC solution is highly sensitive to how the rays intersect the thin layer. Figure 2 demonstrates this sensitivity visually. In both the left and the right cases, three characteristic rays are traced through the problem geometry at the same angle. The rectangles in each case represent the length of the ray that intersects the IFBA region. In the case on the left, a ray tangentially bisects the IFBA layer, while the case on the right is shifted slightly so that no ray tangentially skims the region but intersects it at two points. Since the IFBA region is so highly absorbing, the solution of these two different tracks would vary greatly. Therefore, the MOC solution depends on how the rays are traced across the problem space. The only way to ensure that this dependence is avoided is to narrow the ray spacing down to the size of the IFBA layer. With layers approximately 0.001 cm thick, this would vastly increase the computation time, reducing one of the advantages of using MOC. For full core MOC

calculations, like those done by CASL, this is not a valid option because the computational requirement would be too great.

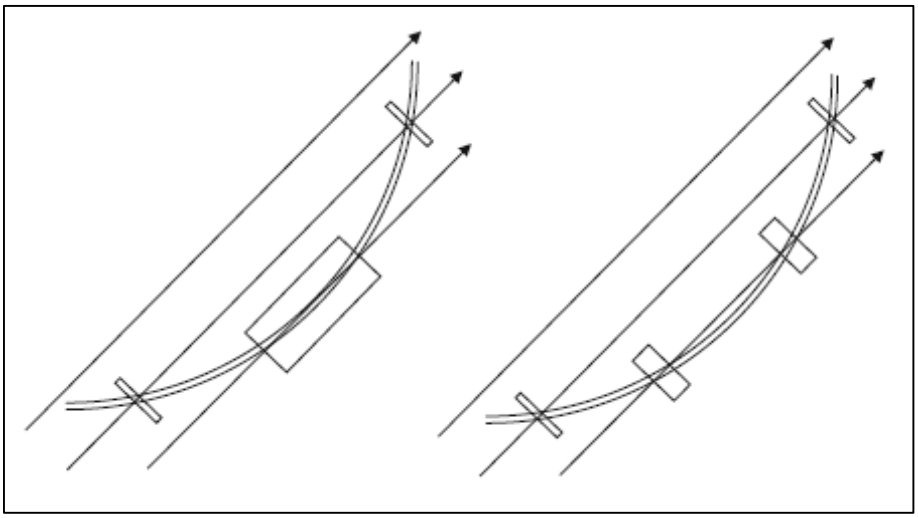

Figure 2. Characteristic tracks intersecting the IFBA layer *[4]*

1.2 Open Literature Search

In order to avoid duplicating prior research, a literary search was conducted to see how IFBA was treated in other studies. Thirteen scientific databases available to the University of Tennessee libraries were searched in addition to general scholarly internet searches. Pramuditya and Takahashi studied modeling integral PWRs using the SRAC code system developed by the Japan Atomic Energy Agency [5]. SRAC utilizes both collision probability and S_N transport solvers as well as diffusion solvers [6]. In this study, IFBA was modeled by smearing the ZrB_2 into the gap between the inner wall of the clad and the fuel. Similarly, there are two studies by Pevec et al. that also smear the IFBA material into the gap [7] [8]. In these studies, the CORD-2 transport code [9] and the FA2D 2D transport collision probability code were used. However, none of these studies mention the effect that smearing the IFBA into the gap has on the localized pin power distribution. A study was performed by Gergeta using the PSU-LEOPARD code in which the explicitly modeled IFBA layer was substituted with the equivalent soluble boron concentration that had the same negative relativity effect as the IFBA [10]. This method is undesirable because, while the overall effective multiplication factor might remain the same, the pin power distribution will be altered greatly. This is because the IFBA layer is meant to be a local neutron suppressant, and when it is removed and spread evenly throughout the coolant, that effect is lost. A study done by Rosa et al. looked at modeling IFBA explicitly using unstructured meshes in a 2D S_N code [11]. While the unstructured mesh approach appears to be faster than a standard structured mesh, it still took 17.5 minutes for a single IFBA pin cell calculation, which is much too long for practical reactor analysis. There were, however, no reports found that discuss modeling IFBA explicitly using MOC. Commercial codes such as CASMO and ANC9 have developed proprietary methods for treating IFBA.

1.3 Research Goals

Despite the lack of solutions put forth by studies available in open literature, there are a few possible solutions that were considered in this report. Two possible solutions are suggested by Knott and Yamamoto [4]. The first possible solution entails homogenizing the thin region with the fuel. The resulting homogenized cross sections are then applied to both the fuel and the IFBA regions. However, this method requires performing a pin cell spectral calculation on the explicit geometry first in order to condense the cross sections. Then, in order to preserve reaction rates in the pin cell, flux and volume weighting are used to homogenize the two regions. The second method put forth is called the macro-band approach. Rather than tracing characteristic rays across the entire problem geometry, the macro-band approach traces rays over each pin cell independently. This idea is shown graphically in Figure 3. In this approach, characteristics are not forced to align at cell boundaries, and the incoming flux of a neighboring cell is linearly interpolated from the two closest outgoing rays. Therefore, IFBA pin cells could have a finer ray spacing than the other regular pins in the problem. This would result in accurately capturing the effect of IFBA on pin powers without a significant increase in run time. The macro-band approach could be used to refine the ray spacing only between the two rays that bookshelf the thin IFBA region, making it even less computationally intensive.

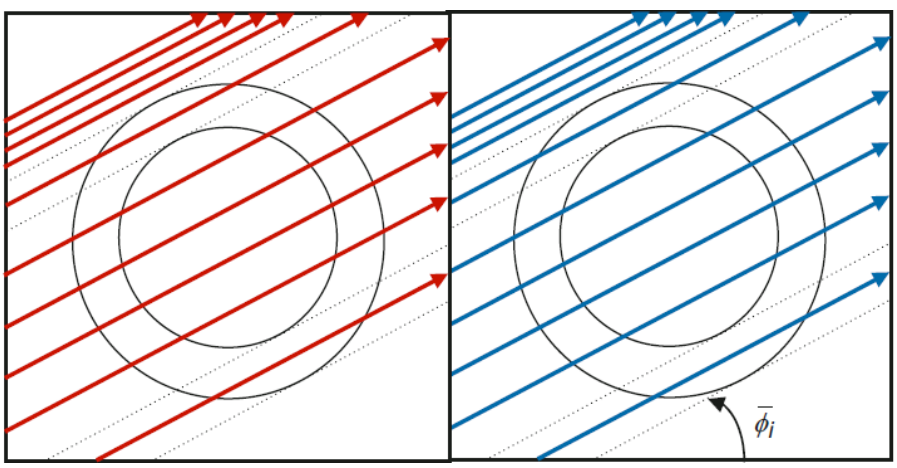

Figure 3. Macro-band approach *[4]*

Group dependent angular quadrature is a possible solution that is similar to the macro-band approach, but instead of refining based on geometry, the ray spacing and angular discretization are refined for the energy groups that are most affected by the IFBA region. The optimum method might consist of a combination of the macro-band approach and a group dependent angular quadrature. Another possible solution consists of determining if the IFBA homogenization factors can be functionalized as a function of a lattice parameter such as burnup or pin location. A table could then be generated and the error introduced by homogenization could be accounted for.

The goal of this work is to make a recommendation for treating IFBA in MOC that gives reasonable accuracy with the least amount of computational requirements.

1.4 MPACT

MPACTs implementation [12] of MOC begins with the steady state continuous form of the Boltzmann neutron transport equation, given by

$$\begin{aligned}\hat{\Omega}\cdot\nabla\varphi(\vec{r},\hat{\Omega},E)+\Sigma_t(\vec{r},E)\varphi(\vec{r},\hat{\Omega},E)\\ =\frac{\chi(\vec{r},E)}{4\pi k_{eff}}\int_0^{\infty}\nu\,\Sigma_f(\vec{r},E')\int_0^{4\pi}\varphi(\vec{r},\hat{\Omega}',E')d\hat{\Omega}'dE'\\ +\int_0^{\infty}\int_0^{4\pi}\Sigma_s(\vec{r},\hat{\Omega}'\cdot\hat{\Omega},E'\to E)\,\varphi(\vec{r},\hat{\Omega}',E')\,d\hat{\Omega}'dE',\end{aligned} \tag{1}$$

where υ is the average number of neutrons released per fission, $\chi(E)$ is the fission neutron energy spectrum, and k_{eff} is the effective multiplication factor. $\varphi(\vec{r},\hat{\Omega},E)$ is the angular neutron flux, such that $\varphi(\vec{r},\hat{\Omega},E)d\vec{r}\,d\hat{\Omega}\,dE$ is the number of neutrons passing through volume element $d\vec{r}$ about $\vec{r}$, moving in solid angle $d\hat{\Omega}$ about direction $\hat{\Omega}$, and with energy dE about E. In Equation (1), $\Sigma_t(\vec{r},E)$ and $\Sigma_f(\vec{r},E')$ are the total and fission macroscopic cross sections, respectively, and $\Sigma_s(\vec{r},\hat{\Omega}'\cdot\hat{\Omega},E'\to E)$ is the macroscopic scattering cross section from direction $\hat{\Omega}'$ and energy E' to direction $\hat{\Omega}$ and energy E. The right hand side of Equation (1) can be rewritten as the total angular neutron source, $Q(\vec{r},\hat{\Omega},E)$, leading to

$$\hat{\Omega}\cdot\nabla\varphi(\vec{r},\hat{\Omega},E)+\Sigma_t(\vec{r},E)\varphi(\vec{r},\hat{\Omega},E)=Q(\vec{r},\hat{\Omega},E). \tag{2}$$

The method of characteristics is applied to Equation (2) which transforms the spatial and angular variables into the characteristic direction using

$$\vec{r}=\vec{r}_0+s\hat{\Omega}\begin{cases}x(s)=x_0+s\Omega_x\\ y(s)=y_0+s\Omega_y\\ z(s)=z_0+s\Omega_z\end{cases}. \tag{3}$$

This leads to the characteristic form of Equation (2), given by

$$\begin{aligned}\frac{d\varphi}{ds}(\vec{r}_0+s\hat{\Omega},\hat{\Omega},E)+\Sigma_t(\vec{r}_0+s\hat{\Omega},E)\varphi(\vec{r}_0+s\hat{\Omega},\hat{\Omega},E)\\ =Q(\vec{r}_0+s\hat{\Omega},\hat{\Omega},E),\end{aligned} \tag{4}$$

where

$$
\begin{aligned}
&Q\left(\vec{r}_0 + s\hat{\Omega}, \hat{\Omega}, E\right) \\
&\qquad = \frac{\chi\left(\vec{r}_0 + s\hat{\Omega}, E\right)}{4\pi k_{eff}} \int_0^{\infty} \int_0^{4\pi} \nu\, \Sigma_f\left(\vec{r}_0 + s\hat{\Omega}', E'\right) \varphi\left(\vec{r}_0 + s\hat{\Omega}', \hat{\Omega}', E'\right) d\hat{\Omega}' dE' \\
&\qquad + \int_0^{\infty} \int_0^{4\pi} \Sigma_s\left(\vec{r}_0 + s\hat{\Omega}, \hat{\Omega}' \cdot \hat{\Omega}, E' \to E\right) \varphi\left(\vec{r}_0 + s\hat{\Omega}', \hat{\Omega}', E'\right) d\hat{\Omega}' dE'.
\end{aligned} \tag{5}
$$

Equation (4) can be solved analytically using the integrating factor

$$
\exp\left(-\int_0^{s} \Sigma_t\left(\vec{r}_0 + s'\hat{\Omega}, E\right)\, ds'\right), \tag{6}
$$

resulting in

$$
\begin{aligned}
\varphi\left(\vec{r}_0 + s\hat{\Omega}, \hat{\Omega}, E\right) &= \varphi\left(\vec{r}_0, \hat{\Omega}, E\right) \exp\left(-\int_0^{s} \Sigma_t\left(\vec{r}_0 + s'\hat{\Omega}, E\right)\, ds'\right) \\
&+ \int_0^{s} Q\left(\vec{r}_0 + s\hat{\Omega}, \hat{\Omega}, E\right) \exp\left(-\int_{s'}^{s} \Sigma_t\left(\vec{r}_0 + s''\hat{\Omega}, E\right)\, ds''\right) ds'.
\end{aligned} \tag{7}
$$

Therefore, Equation (7) is the steady state solution of the characteristics form of the Boltzmann neutron transport equation.

1.4.1 Multigroup Approximation

In order to solve Equation (7) numerically, some appropriate approximations must be made in order to discretize the continuous variables in the integrals. The first discretization to be described is the multigroup approximation. This discretizes the continuous energy variable, E, for which the multigroup cross sections are a constant for a given group, g. These multigroup cross sections can be determined exactly for a given reaction type, x, using

$$
\Sigma_{x,g}(\vec{r}) = \frac{\int_{E_g}^{E_{g-1}} \Sigma_x(\vec{r}, E) \int_{4\pi} \varphi\left(\vec{r}, \hat{\Omega}, E\right) dE\, d\Omega}{\int_{E_g}^{E_{g-1}} \int_{4\pi} \varphi\left(\vec{r}, \hat{\Omega}, E\right) dE\, d\Omega}. \tag{8}
$$

However, the angular neutron flux, $\varphi\left(\vec{r}, \hat{\Omega}, E\right)$, is usually not known when making the multigroup approximation. Therefore an approximation is made assuming that $\varphi\left(\vec{r}, \hat{\Omega}, E\right)$ is separable:

$$
\varphi\left(\vec{r}, \hat{\Omega}, E\right) \approx \Psi(\vec{r}, E) f\left(\vec{r}, \hat{\Omega}\right). \tag{9}
$$

$\Psi(\vec{r}, E)$ is a weighting factor in energy and should be selected to represent the neutron energy spectrum of the problem. Even though this is usually not known prior to solving the problem, this separation approximation is valid for collapsing the continuous energy cross sections as long

as $\Psi(\vec{r},E)$ is reasonably consistent with the energy distribution in the problem. Substituting Equation (9) into Equation (8) yields

$$\Sigma_{x,g}(\vec{r}) \approx \frac{\int_{E_g}^{E_{g-1}} \Sigma_x(\vec{r},E)\Psi(\vec{r},E)dE}{\int_{E_g}^{E_{g-1}} \Psi(\vec{r},E)dE}. \tag{10}$$

The fission neutron energy spectrum for a given group, g, is given by

$$\chi_g(\vec{r}) = \int_{E_g}^{E_{g-1}} \chi(\vec{r},E)dE. \tag{11}$$

Using these approximations with Equation (7) and Equation (5) leads to the multigroup solution of the characteristics form of the Boltzmann transport equation, given by

$$\begin{aligned}\varphi_g(\vec{r}_0 + s\hat{\Omega},\hat{\Omega}) = \varphi_g(\vec{r}_0,\hat{\Omega}) \exp\left(-\int_0^s \Sigma_{t,g}(\vec{r}_0 + s'\hat{\Omega})\ ds'\right) \\ + \int_0^s Q_g(\vec{r}_0 + s\hat{\Omega},\hat{\Omega}) \exp\left(-\int_{s'}^s \Sigma_{t,g}(\vec{r}_0 + s''\hat{\Omega})\ ds''\right) ds'\end{aligned} \tag{12}$$

and

$$\begin{aligned}Q_g(\vec{r}_0 + s\hat{\Omega},\hat{\Omega}) \\ = \frac{\chi_g(\vec{r}_0 + s\hat{\Omega})}{4\pi k_{eff}} \sum_{g'=1}^{G} \int_0^{4\pi} \nu\, \Sigma_{f,g'}(\vec{r}_0 + s\hat{\Omega}')\varphi_{g'}(\vec{r}_0 + s\hat{\Omega}',\hat{\Omega}')d\hat{\Omega}' \\ + \sum_{g'=1}^{G} \int_0^{4\pi} \Sigma_{s,g'\to g}(\vec{r}_0 + s\hat{\Omega},\hat{\Omega}'\cdot\hat{\Omega})\, \varphi_{g'}(\vec{r}_0 + s\hat{\Omega}',\hat{\Omega}')d\hat{\Omega}'.\end{aligned} \tag{13}$$

1.4.2 The Discrete Ordinates Approximation

The next discretization to be described is the discrete ordinates approximation which discretizes the continuous angular variable $\hat{\Omega}$. This is done using a quadrature, which approximates the definite integral of a function of angle as a weighted sum of the function at specific values, given by

$$\int_{4\pi} f(\hat{\Omega})d\Omega \approx \sum_{m=1}^{M} w_m f(\hat{\Omega}_m). \tag{14}$$

Substituting this approximation into Equation (12) and Equation (13) yields

$$\varphi_{g,m}(\vec{r}_0 + s\widehat{\Omega}_m) = \varphi_{g,m}(\vec{r}_0)\exp\left(-\int_0^s \Sigma_{t,g}(\vec{r}_0 + s'\widehat{\Omega}_m)\ ds'\right) + \int_0^s Q_{g,m}(\vec{r}_0 + s\widehat{\Omega}_m)\exp\left(-\int_{s'}^s \Sigma_{t,g}(\vec{r}_0 + s''\widehat{\Omega}_m)\ ds''\right)ds', \tag{15}$$

where

$$Q_{g,m}(\vec{r}_0 + s\widehat{\Omega}_m) = \frac{\chi_g(\vec{r}_0 + s\widehat{\Omega}_m)}{4\pi k_{eff}}\sum_{g'=1}^{G}\sum_{m'=1}^{M} \nu\,\Sigma_{f,g'}(\vec{r}_0 + s\widehat{\Omega}_{m'})w_{m'}\varphi_{g',m'}(\vec{r}_0 + s\widehat{\Omega}_{m'}) + \sum_{g'=1}^{G}\sum_{m'=1}^{M} w_{m'}\,\Sigma_{s,g'\to g}(\vec{r}_0 + s\widehat{\Omega}_{m'}, \widehat{\Omega}_{m'}\cdot\widehat{\Omega}_m)\varphi_{g',m'}(\vec{r}_0 + s\widehat{\Omega}_{m'})\,. \tag{16}$$

The discrete ordinates approximation is found to be accurate as long as a sufficient number of angles are used along with an appropriate choice of w_m and $\widehat{\Omega}_m$.

1.4.3 Spatial Discretization

The problem to be modeled is divided into discrete regions in order to discretize the spatial variable. The material properties are assumed to be constant for a given spatial region. This assumption is found to be first order accurate. If characteristic ray k is passing through discrete region i, then Equation (15) and Equation (16) are reduced to

$$\varphi_{i,g,m,k}^{out} = \varphi_{i,g,m,k}^{in}\exp(-\Sigma_{t,i,g}s_{i,m,k}) + \int_0^{s_{i,m,k}} Q_{i,g,m}(s')\exp\left(-\Sigma_{t,i,g}(s_{i,m,k} - s')\right)ds' \tag{17}$$

and

$$Q_{i,g,m}(s) = \frac{\chi_{i,g}}{4\pi k_{eff}}\sum_{g'=1}^{G}\nu\Sigma_{f,i,g'}\sum_{m'=1}^{M} w_{m'}\varphi_{i,g',m'}(s) + \sum_{g'=1}^{G}\sum_{m'=1}^{M} w_{m'}\,\Sigma_{s,i,g'\to g}(\widehat{\Omega}_{m'}\cdot\widehat{\Omega}_m)\varphi_{i,g',m'}(s)\,, \qquad 0 \le s \le s_{i,m,k} \tag{18}$$

where

$$\varphi_{i,g,m,k}^{in} = \varphi_{i,g,m}(\vec{r}_0) = \varphi_{i,g,m,k}(s = 0) \text{ and}$$
$$\varphi_{i,g,m,k}^{out} = \varphi_{i,g,m}(\vec{r}_0 + s_{i,m,k}\widehat{\Omega}_m) = \varphi_{i,g,m,k}(s = s_{i,m,k})\,.$$

For neighboring discrete regions i and $i+1$, the outgoing flux in region i equals the incoming flux in region $i+1$ along ray k, for energy group g, in direction m.

It can also be assumed that the neutron source, Q, is constant within each discretized region. This is known as the flat source approximation. The flat source approximation is found to be accurate as long as a fine enough spatial mesh is used. With this approximation, Equation (17) and Equation (18) can be simplified by evaluating the remaining integral, leading to

$$\varphi_{i,g,m,k}^{out} = \varphi_{i,g,m,k}^{in} \exp\left(-\Sigma_{t,i,g} s_{i,m,k}\right) + \frac{Q_{i,g,m}}{\Sigma_{t,i,g}} \left[1 - \exp\left(-\Sigma_{t,i,g} s_{i,m,k}\right)\right] \tag{19}$$

and

$$\begin{aligned} Q_{i,g,m} = \frac{\chi_{i,g}}{4\pi k_{eff}} \sum_{g'=1}^{G} \nu\Sigma_{f,i,g'} \sum_{m'=1}^{M} w_{m'} \bar{\varphi}_{i,g',m'} \\ + \sum_{g'=1}^{G} \sum_{m'=1}^{M} w_{m'} \Sigma_{s,i,g'\to g}\left(\hat{\Omega}_{m'} \cdot \hat{\Omega}_{m}\right) \bar{\varphi}_{i,g',m'}. \end{aligned} \tag{20}$$

The region average angular flux, $\bar{\varphi}_{i,g,m}$, in Equation (20) is found from

$$\bar{\varphi}_{i,g,m} = \frac{\sum_{k\in i} \tilde{\varphi}_{i,g,m,k}\, s_{i,m,k} \delta A_{m,k}}{\sum_{k\in i} s_{i,m,k} \delta A_{m,k}}, \tag{21}$$

where $\delta A_{m,k}$ represents the cross sectional area of the characteristic ray k in direction m, and where $\tilde{\varphi}_{i,g,m,k}$ is the segment average angular flux, given by

$$\tilde{\varphi}_{i,g,m,k} = \frac{\int_0^{s_{i,m,k}} \varphi_{i,g,m}(s')ds'}{\int_0^{s_{i,m,k}} ds'} \Longrightarrow \frac{\varphi_{i,g,m,k}^{in} - \varphi_{i,g,m,k}^{out}}{\Sigma_{t,i,g} s_{i,m,k}} + \frac{Q_{i,g,m}}{\Sigma_{t,i,g}}. \tag{22}$$

Therefore, Equation (22) and Equation (19) must be solved in order to obtain the angular neutron flux for the modeled problem.

1.4.4 Segment Length

In order to evaluate Equation (19) and Equation (22), the segment lengths for each characteristic ray passing through each discrete region, $s_{i,m,k}$, must be determined. This is done by storing the ray tracing data, which includes the intersection between the rays and the discrete spatial region boundaries. These segment lengths multiplied by the segment cross section, $\delta A_{m,k}$, represent an integration of the region volume. In order to integrate the region volume exactly, the segment lengths within a given region are renormalized using

$$\bar{s}_{i,m,k} = s_{i,m,k} \frac{V_i}{\sum_{k\in i} s_{i,m,k} \delta A_{m,k}}. \tag{23}$$

2. Models

2.1 2D IFBA Pin Cell

In order to gain insight into the problem of modeling IFBA using MOC, CASL VERA Core Physics Benchmark Problem 1E [13], which is a single 2D Hot Zero Power (HZP) IFBA pin cell at Beginning of Life (BOL), was modeled using MPACT. Due to reflective boundary conditions, this 2D pin cell model can be thought of as being a single, infinitely tall fuel rod in a square coolant channel within an infinite array of pins. This simple model consists of only five regions consisting of five standard materials: a UO_2 fuel pellet, a helium gap, a Zircaloy-4 cladding, a ZrB_2 IFBA layer, and borated water as the surrounding coolant and moderator. The operating conditions and input specifications are shown in Table 1. These input parameters were taken from the VERA Core Physics Benchmark Problem Specifications [13]. A 2D representation of a fuel pin cell is shown in Figure 4.

Table 1: 2D pin cell input specifications *[13]*

Parameter	Value
Moderator Temperature	600 K
Moderator Density	0.743 g/cc
Fuel Temperature	600 K
Fuel Density	10.257 g/cc
Fuel Enrichment	3.10%
Power	0%
Boron Concentration	1300 ppm
Pin Pitch	1.26 cm
Fuel Radius	0.4096 cm
IFBA Thickness	0.001 cm
Gap Thickness	0.0074 cm
Clad Thickness	0.057 cm

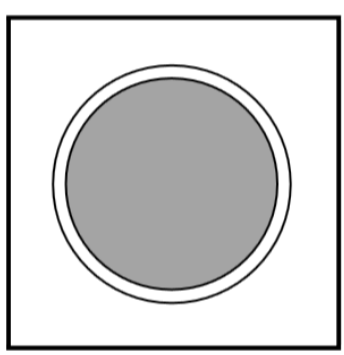

Figure 4. 2D representation of a pin cell *[13]*

2.2 2D IFBA Lattice

Next, CASL VERA Core Physics Benchmark Problem 2M [13], which is a two-dimensional array of fuel rods, was modeled at BOL under HZP conditions. This single assembly model is a 17x17 lattice with 264 fuel pins, 128 of which contain IFBA. There are also 24 guide tubes for inserting control rods and one instrument tube located at the lattice center. The interior of the guide tubes and instrument tube are filled with moderator. The operating conditions and the 128 IFBA rods follow the specifications in Table 1, while the rest of the modeled assembly specifications are shown in Table 2. A quarter assembly representation of this geometry is displayed in Figure 5, where the IFBA rods are brown and the non-IFBA rods are shown as red.

Table 2: 2D lattice additional input specifications *[13]*

Parameter	Value
Assembly Pitch	21.50 cm
Guide Tube Inner Radius	0.561 cm
Guide Tube Outer Radius	0.602 cm
Non-IFBA Gap Thickness	0.0084 cm

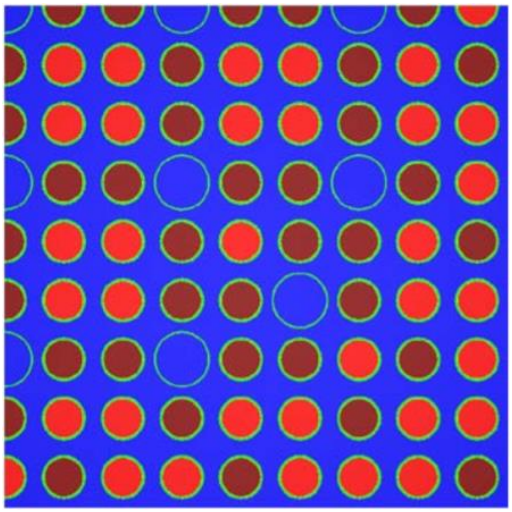

Figure 5. 2D IFBA quarter assembly geometry *[13]*

2.3 2D Full Core AP1000 Midplane

An AP1000® full core 2D midplane at BOL was used to test IFBA in large scale problems. BOL cases have the largest IFBA population because as the problem depletes, so does the IFBA layer. Therefore, BOL cases are expected to be more difficult to model than later fuel cycles. The

AP1000 model was generated using data publicly available from the CASL report on the Westinghouse VERA Test Stand [14]. The input specifications of the AP1000 are shown in Table 3. An important difference between the AP1000 and the prior models is that the IFBA layer is now on the order of 0.0005 cm thick.

Table 3: AP1000 input specifications *[14]*

Parameter	Value
Moderator Temperature	565 K
Moderator Density	0.7441292 g/cc
Fuel Temperature	565 K
Fuel Density	10.28 g/cc
Power	0%
Boron Concentration	1321 ppm
Assembly Pitch	21.50 cm
Pin Pitch	1.26 cm
Fuel Radius	0.409575 cm
IFBA Thickness	0.000508 cm
IFBA Pin Gap Thickness	0.007747 cm
Non-IFBA Pin Gap Thickness	0.008255 cm
Clad Thickness	0.05715 cm
Guide Tube Inner Radius	0.56134 cm
Guide Tube Outer Radius	0.61214 cm

The core consists of 157 assemblies and was modeled using quarter core symmetry. Figure 6 below shows a map of the assembly configuration in quarter symmetry.

2	4	2	4	2	4	5	3
4	2	4	2	4	2	5	1
2	4	2	4	2	5	3	
4	2	4	2	5	3	1	
2	4	2	5	2	3		
4	2	5	3	3			
5	5	3	1				
3	1						

Figure 6. AP1000 assembly map in quarter symmetry

The different numbers and colors correspond to assemblies with differing fuel enrichments. The larger assembly numbers represent higher U-235 enrichments in the assembly. The corresponding fuel enrichments are shown in Table 4.

Table 4. AP1000 fuel enrichments by region

Assembly Number	Enrichment
1	0.74%
2	1.58%
3	3.20%
4	3.40%, 3.80%, 4.20%
5	4.00%, 4.40%, 4.80%

Regions 4 and 5 contain three different fuel enrichments, low (L) medium (M) and high (H), in the same configuration. This configuration in quarter assembly symmetry is shown in Figure 7. The center pin is the instrument tube, represented by IT, and contains no fuel. Also, there are 24 guide tubes, represented by a G, that are used for inserting control rod banks or discrete burnable absorber rods.

IT	M	M	G	M	M	G	M	L
M	H	H	M	H	H	M	M	L
M	H	H	M	H	H	M	M	L
G	M	M	G	M	M	G	M	L
M	H	H	M	M	M	M	M	L
M	H	H	M	M	G	M	M	L
G	M	M	G	M	M	M	M	L
M	M	M	M	M	M	M	M	L
L	L	L	L	L	L	L	L	L

Figure 7. Assembly fuel enrichment configuration for regions 4 and 5 in quarter symmetry

In addition to the use of IFBA as a burnable absorber in the AP1000, Wet Annular Burnable Absorbers (WABA) are also used. WABA are burnable poisons that contain B_4C-Al_2O_3 and are placed within the guide tubes of a lattice. WABA is annular, with moderator in the middle, an inner Zircaloy-4 clad and helium gap, the poison, and then an outer helium gap and Zircaloy-4 clad. The specification of the modeled WABA dimensions are shown in Table 5 and a diagram of the WABA configuration is shown in Figure 8.

Table 5: WABA burnable poison specification

Parameter	Value
Inner Clad Inner Radius	0.29 cm
Inner Clad Outer Radius	0.34 cm
Poison Inner Radius	0.35 cm
Poison Outer Radius	0.40386 cm
Outer Clad Inner Radius	0.41783 cm
Outer Clad Outer Radius	0.48387 cm
Cladding Material	Zircaloy-4
Gap Material	Helium

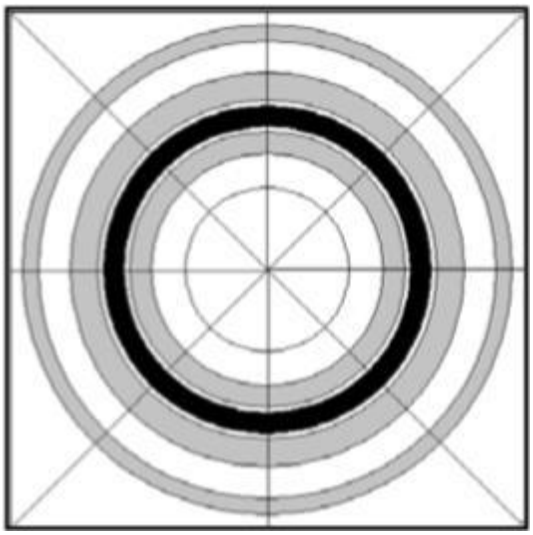

Figure 8. WABA geometry in 2D *[13]*

Both IFBA and WABA are used as burnable absorbers in this AP1000 model. There are three different IFBA configurations that are used that contain 68, 88, or 124 IFBA rods. These three configurations are shown in Figure 9. There are also three different WABA configurations that contain 4, 8, or 12 WABA rods. These three configurations are shown in Figure 10. The different IFBA and WABA configurations are placed in the core in varying combinations. These burnable poison combinations are shown in Figure 11.

-	I							
-	-	I						
	-	-						
-	-	I	-	-				
-	-	I	-	-				
	-	-		-	-	-		
-	-	-	I	-	-	-	I	
I	-	I	-	I	-	I	-	I

-	-							
-	-	-						
	-	-						
-	-	I	-	-				
-	-	I	-	-				
	-	-		-	-	-		
I	-	I	I	-	-	-	-	
I	I	I	I	I	I	-	I	-

-	I							
-	-	-						
	-	-						
-	-	I	-	-				
-	I	I	-	-				
	-	-		I	-	-		
I	-	I	I	-	-	-	I	
I	I	I	I	I	I	I	I	I

Figure 9. 68 (left), 88 (middle), and 124 (right) IFBA configurations in octant symmetry

-	-							
-	-	-						
	-	-	W					
-	-	-	-	-				
-	-	-	-	-				
	-	-		-	-	-		
-	-	-	-	-	-	-	-	
-	-	-	-	-	-	-	-	-

-	-							
-	-	-						
W	-	-						
-	-	-	-	-				
-	-	-	-	-	W			
	-	-		-	-	-		
-	-	-	-	-	-	-	-	
-	-	-	-	-	-	-	-	-

-	-							
-	-	-						
W	-	-						
-	-	-	-	-				
-	-	-	-	-	W			
W	-	-		-	-	-		
-	-	-	-	-	-	-	-	
-	-	-	-	-	-	-	-	-

Figure 10. 4 (left), 8 (middle), 12 (right) WABA configurations in octant symmetry

2	68I 4 12W	2	68I 4 12W	2	68I 4 12W	124I 5	3
68I 4 12W	2	68I 4 12W	2	68I 4 12W	2	88I 5 4W	1
2	68I 4 12W	2	68I 4 12W	2	124I 5 8W	3	
68I 4 12W	2	68I 4 12W	2	124I 5 8W	3	1	
2	68I 4 12W	2	124I 5 8W	2	3		
68I 4 12W	2	124I 5 8W	3	3			
124I 5	88I 5 4W	3	1				
3	1						

Figure 11. IFBA and WABA burnable absorber placement in AP1000 quarter core

2.4 Extreme Case

In order to determine if the effect of ray spacing on the eigenvalue is amplified by an increased presence of IFBA, an extreme case was run in which every other assembly in the AP1000 2D core slice was made entirely out of IFBA rods. The WABA pattern remained the same in this case, but all 264 fuel pins in every other assembly were 4.20% enriched IFBA rods. This core assembly layout is shown in Figure 12. All other core parameters remained the same between this extreme case and the standard AP1000 input described in Section 2.3.

2	264I 4 12W	2	264I 4 12W	2	264I 4 12W	124I 5	264I 4
264I 4 12W	2	264I 4 12W	2	264I 4 12W	2	264I 4 4W	1
2	264I 4 12W	2	264I 4 12W	2	264I 4 8W	3	
264I 4 12W	2	264I 4 12W	2	264I 4 8W	3	264I 4	
2	264I 4 12W	2	264I 4 8W	2	264I 4		
264I 4 12W	2	264I 4 8W	3	264I 4			
124I 5	264I 4 4W	3	264I 4				
264I 4	1						

Figure 12. IFBA and WABA burnable absorber placement in extreme case in quarter symmetry

2.5 Volume Weighted Smearing

Many of the references in Section 1.2 treated IFBA by volume weighting the material and then smearing it into the fuel rod gap. To test this method, two models were made in which the standard AP1000 input described in Section 2.3 was modified so that the IFBA material was volume weighted and smeared into both the gap and the clad. In these models, the densities were calculated so that the total number of atoms of both the Zr and the B^{10} in the IFBA would be the same smeared into the new gap or clad volume. In both cases, the IFBA layer is replaced with a more diffuse gap helium in order to keep the number of helium atoms constant.

2.6 Reference Solutions

The results of the 2D IFBA pin cell, lattice, and standard AP1000 cases using MPACT were compared to reference solutions generated in the CASL VERA Core Physics Benchmark Progression Problem Specifications [13] and the CASL report on the Westinghouse VERA Test Stand [14]. These reference solutions were generated using a development version of the SCALE 6.2 code KENO-VI [15]. KENO-IV is a continuous energy (CE) Monte Carlo transport code that uses ENDF/B-VII.0 CE cross sections. KENO-IV models the exact geometry specification and can approximate the eigenvalue solution within a small uncertainty, generally within a few thousandths of a percent. It can also calculate the pin power distribution of a problem by tallying the fission rate in each fuel rod. These reference solutions were used to compare the results outlined in the following section.

3. Results and Discussion

3.1 2D IFBA Pin Cell

To demonstrate the issue of modeling IFBA using MOC, CASL VERA Core Physics Benchmark Problem 1E, which is a single IFBA pin, was run using MPACT with various ray spacings. The effective multiplication factors, k-eff, of these cases were compared to that of a high fidelity CE-KENO reference solution, and the differences are displayed below in Figure 13. The differences are given as percent mille (pcm), or one one-thousandth of a percent. While k-eff differences of less than 200 pcm are acceptable, differences of less than 100 pcm are desired. The finest ray spacing run was 0.001 cm which is also the thickness of the IFBA layer in the problem. As seen in Figure 13, the eigenvalue of this single IFBA pin is highly sensitive to changes in ray spacing. As the ray spacing approaches the IFBA thickness, the rays better resolve the IFBA region and the answer converges closer to the reference solution. Because of the approximations stated in Section 1.4, there are differences expected between the MOC and Monte Carlo solutions. However, refining the ray spacing down to the size of the IFBA region greatly increases the run time. The effect of ray spacing on run time is shown in Figure 14. Running this single pin cell case at a ray spacing of 0.001 cm, which is the thickness of the IFBA, takes 7.6 times longer to run than a the default ray spacing of 0.05 cm. Even though the fine ray spacing took only 25 seconds to run, should this level of ray spacing refinement be required for a full core 2D plane, MPACT calculations involving IFBA would be extremely computationally intensive.

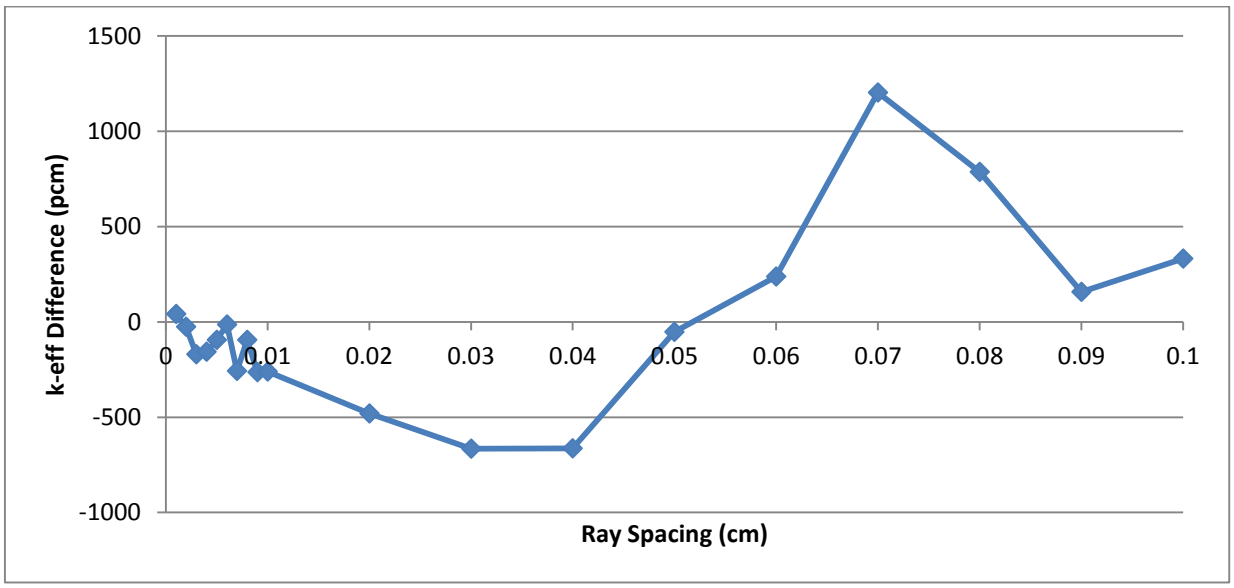

Figure 13. k-eff differences of CASL VERA Core Physics Benchmark Problem 1E at various ray spacings compared to CE-KENO

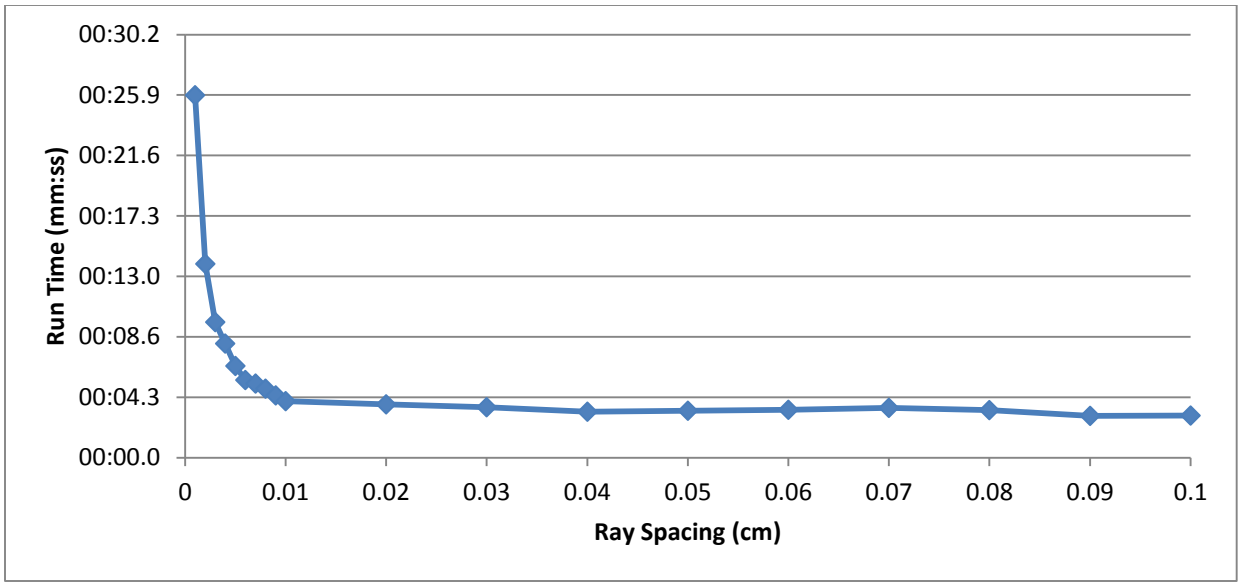

Figure 14. Run time of CASL VERA Core Physics Benchmark Problem 1E at various ray spacings

3.2 2D IFBA Lattice

To see if the difficulty of modeling IFBA using MOC is still apparent on the scale of a single assembly, CASL VERA Core Physics Benchmark Problem 2M, was run using MPACT with various ray spacings. The k-effective of these cases were compared to that of a high fidelity CE-KENO reference solution, and the differences are displayed in Figure 15. While the eigenvalue differences in Figure 15 are smaller than those in Figure 13, they are still very significant around the default ray spacing of 0.05 cm. Therefore a much finer ray spacing would be needed to resolve the effect of IFBA on the lattice eigenvalue.

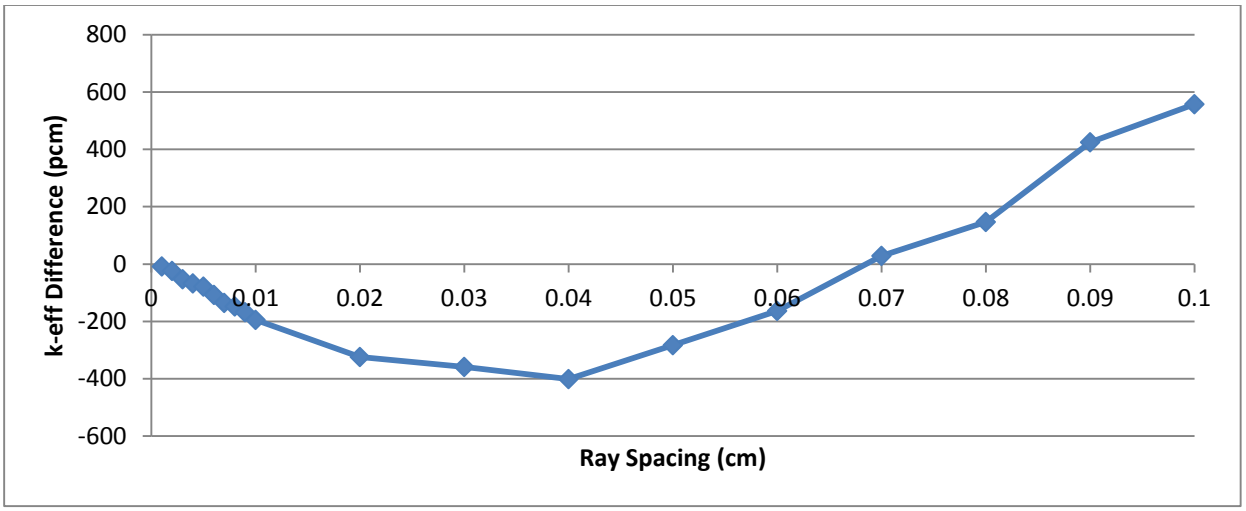

Figure 15. k-eff differences of CASL VERA Core Physics Benchmark Problem 2M at various ray spacings compared to CE-KENO

In addition to the eigenvalue comparison to the KENO reference solution, the relative pin powers were also compared. Both the root mean square (RMS) error as well as the maximum error were calculated for each ray spacing, and are shown together in Figure 16. For modeling and simulation accuracy, it is desired that the RMS differences be less than 0.25% and the maximum differences be less than 0.5%. Therefore, these pin power differences are relatively small for both the fine ray spacings as well as the standard ray spacing. To demonstrate this, a map of the pin power differences calculated at the default ray spacing is shown in Figure 17. When compared to Figure 5, it should be noted that the pins with the largest pin power difference occur in fuel pins not containing IFBA. Therefore, when using the standard ray spacing, IFBA pins are not limiting the pin power accuracy.

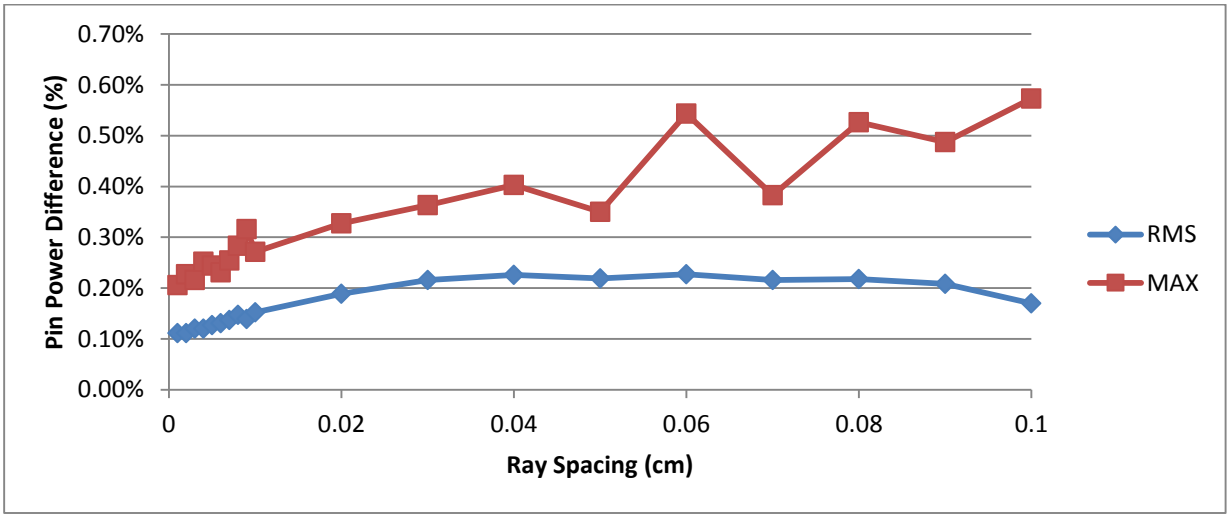

Figure 16. Pin power differences of CASL VERA Core Physics Benchmark Problem 2M at various ray spacings compared to CE-KENO

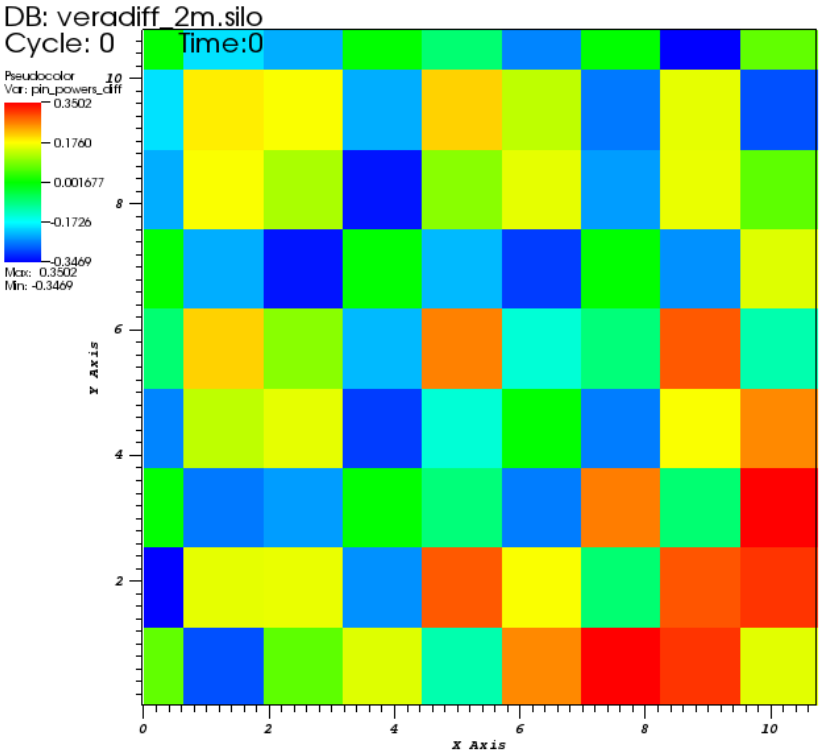

Figure 17. Pin power difference map of CASL VERA Core Physics Benchmark Problem 2M in quarter symmetry between MPACT and CE-KENO using the default ray spacing

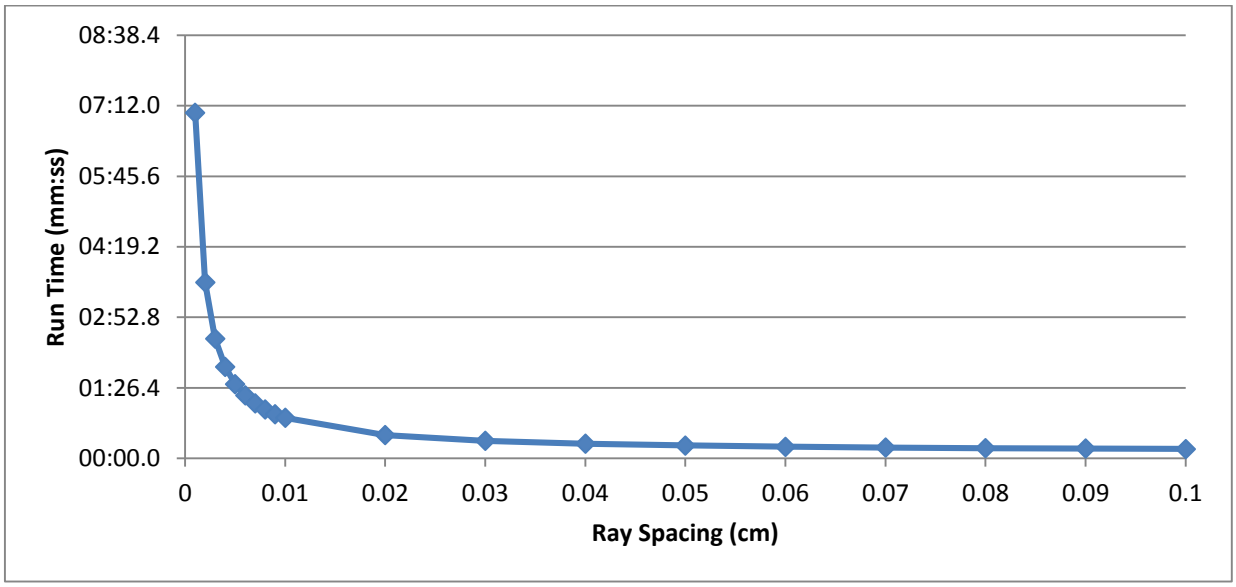

Figure 18. Run time of CASL VERA Core Physics Benchmark Problem 2M at various ray spacings

The effect of ray spacing on run time is shown above in Figure 18. Running a single assembly calculation with the ray spacing the size of the IFBA layer (0.001 cm) takes 27 times longer than running with the standard 0.05 cm ray spacing. This increased run time yields only moderate improvement in pin power, but a significant 400 pcm improvement in eigenvalue.

3.3 2D Full Core AP1000 Midplane

Next, full core calculations were run to see if this effect is as significant on large scale problems as it was on the single pin cell and lattice problems. This AP1000 full core 2D midplane was run using MPACT with various ray spacings. The k-effective of these cases were compared to that of a high fidelity CE-KENO reference solution, and the differences are displayed below in Figure 19. The k-eff differences follow similar trends to that of the single pin cell and lattice calculations. However, the magnitude of the differences is much smaller in the full core case than the other smaller cases.

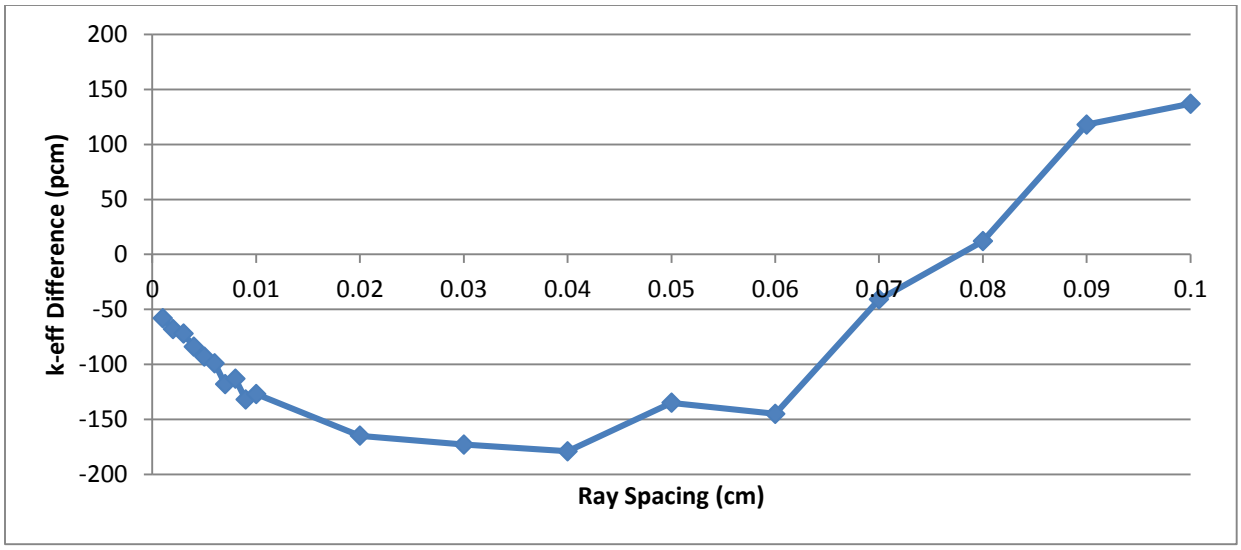

Figure 19. k-eff differences of AP1000 Full Core 2D Plane at various ray spacings compared to CE-KENO

It appears that the effect of ray spacing on IFBA problems of large scale average out, and are not as sensitive as a single pin cell or singe assembly, even though the IFBA layer is 0.000508 cm thick, which is about twice as thin as the other cases. The pin powers of the full core AP1000 2D slice were also calculated and compared to those from CE-KENO. The RMS differences and the maximum pin power differences are shown in Figure 20. For a default ray spacing of 0.05 cm, the maximum pin power difference is less than 1.08% while the RMS difference is less than 0.42%. However, there is little to no improvement gained by running with smaller ray spacings. In fact, this negligible improvement costs an additional 10.6 times increase in run time. The effect of ray spacing on run time is shown in Figure 21.

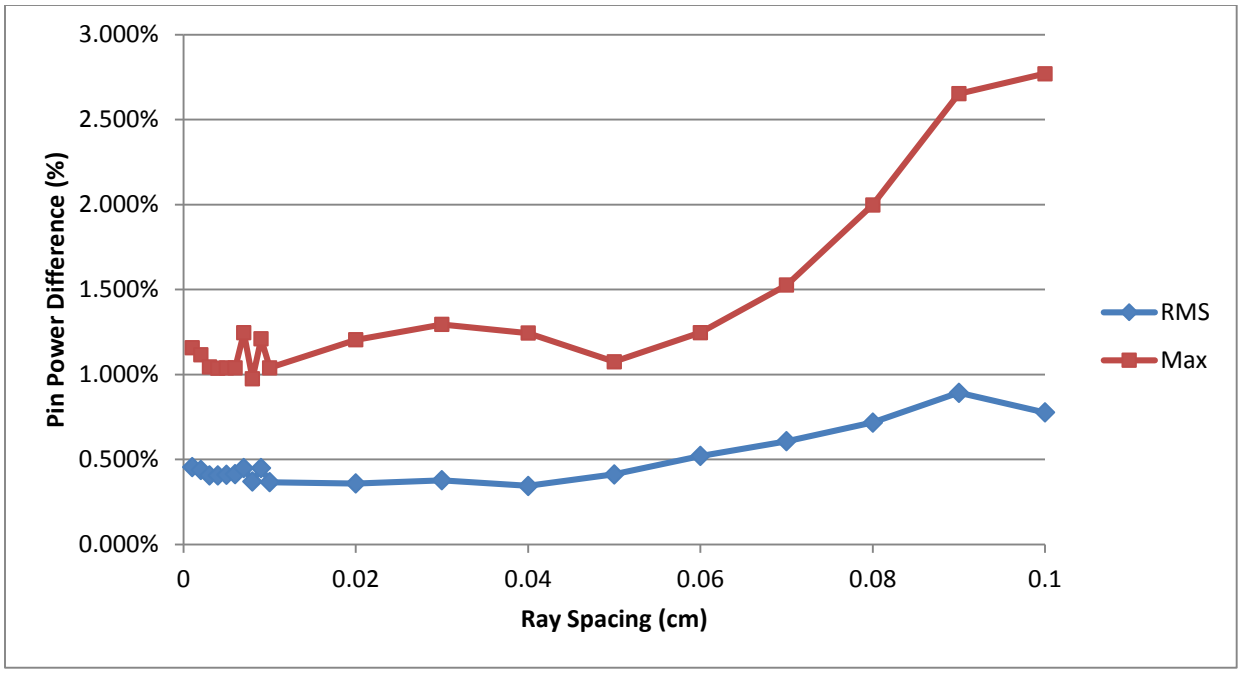

Figure 20. Pin power differences of AP1000 Full Core 2D Plane at various ray spacings compared to CE-KENO

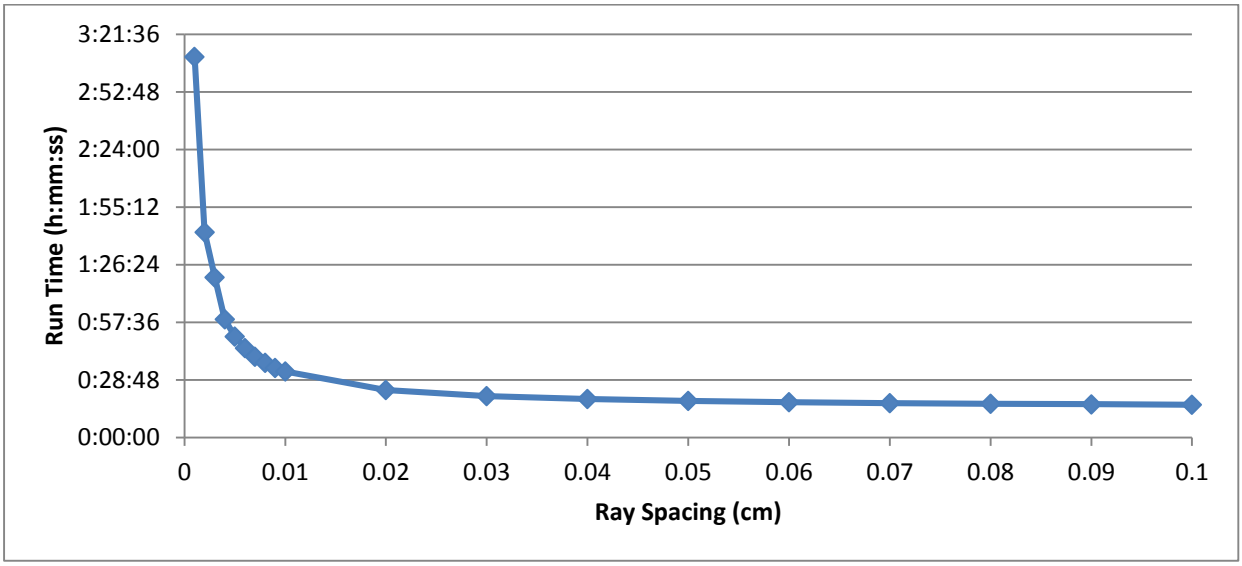

Figure 21. Run time of AP1000 Full Core 2D Plane at various ray spacings

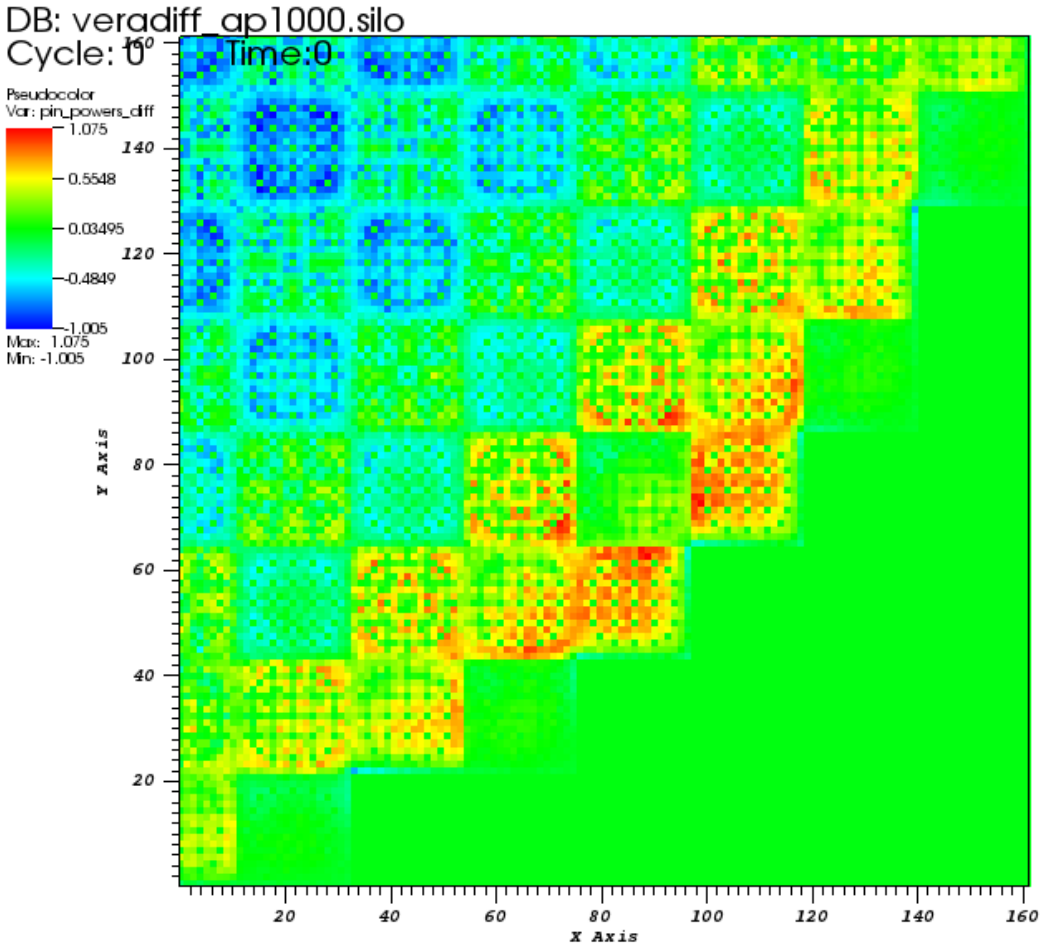

Figure 22. Pin power difference map of AP1000 Full Core 2D Plane in quarter symmetry between MPACT and CE-KENO using the default ray spacing

To examine where the maximum pin power differences occur, a map of the pin power differences calculated at the default ray spacing was generated and is shown in Figure 22. When compared to Figure 11, it should be noted that the pins with the largest pin power difference occur in the assemblies on the outside of the core which do not contain IFBA. Therefore, when using the standard ray spacing, IFBA pins are not limiting the pin power accuracy.

3.4 Extreme Case

An extreme case was run in which every other assembly in the AP1000 2D core slice was made entirely out of IFBA rods. This study was run to determine whether the effect of ray spacing on the eigenvalue is amplified by an increased presence of IFBA. Figure 23 below shows the k-eff difference when compared to the k-eff of the finest ray spacing run, since there is no KENO benchmark for this problem. It can be seen that, while the k-eff difference is larger in this extreme case when compared to the standard AP1000 2D plane at the same ray spacing, the

difference in the area of the default ray spacing (0.05 cm) and smaller is not as large as those seen in the single pin cell or lattice cases.

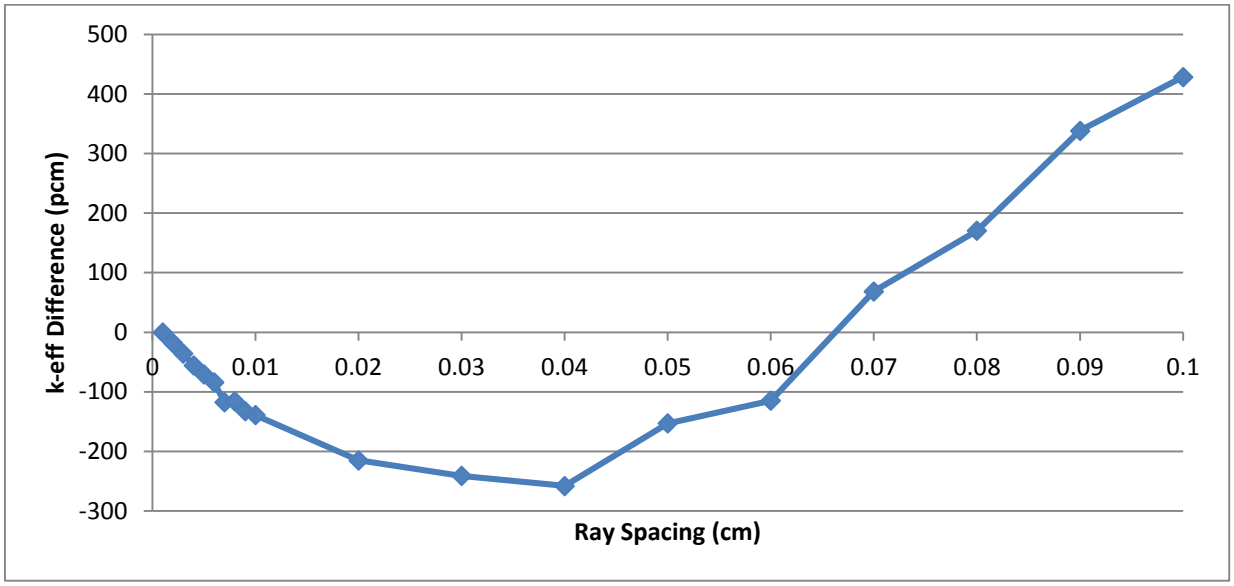

Figure 23. k-eff differences of AP1000 Full Core 2D Plane with every other assembly made entirely of IFBA at various ray spacings compared to 0.001 cm ray spacing

3.5 Volume Weighted Smearing

In order to investigate whether the effect of the IFBA layer could be retained without have to explicitly model the thin region, the IFBA material was homogenized into the surrounding areas, as described in Section 2.5. The IFBA material was weighted by volume and smeared into both the gap and clad regions. These cases were run using MPACT at various ray spacings and the eigenvalues and pin powers were compared to those from CE-KENO. The k-effective differences, pin power RMS differences, and maximum pin power differences are shown below in Figure 24, Figure 25, and Figure 26, respectively, for each of the three cases run.

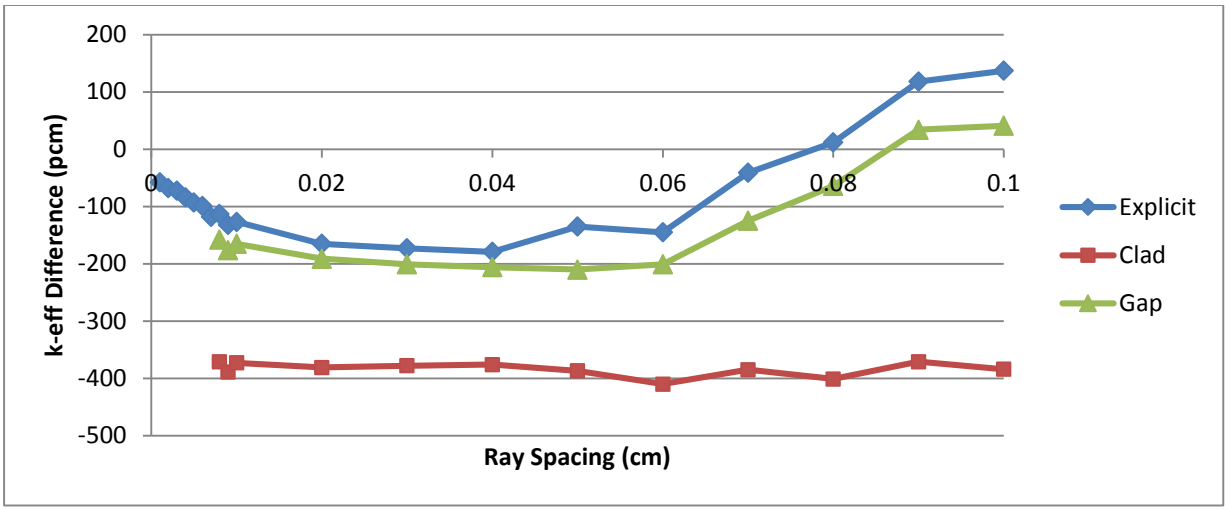

Figure 24. k-eff differences of AP1000 Full Core 2D Plane with smeared IFBA regions at various ray spacings compared to CE-KENO

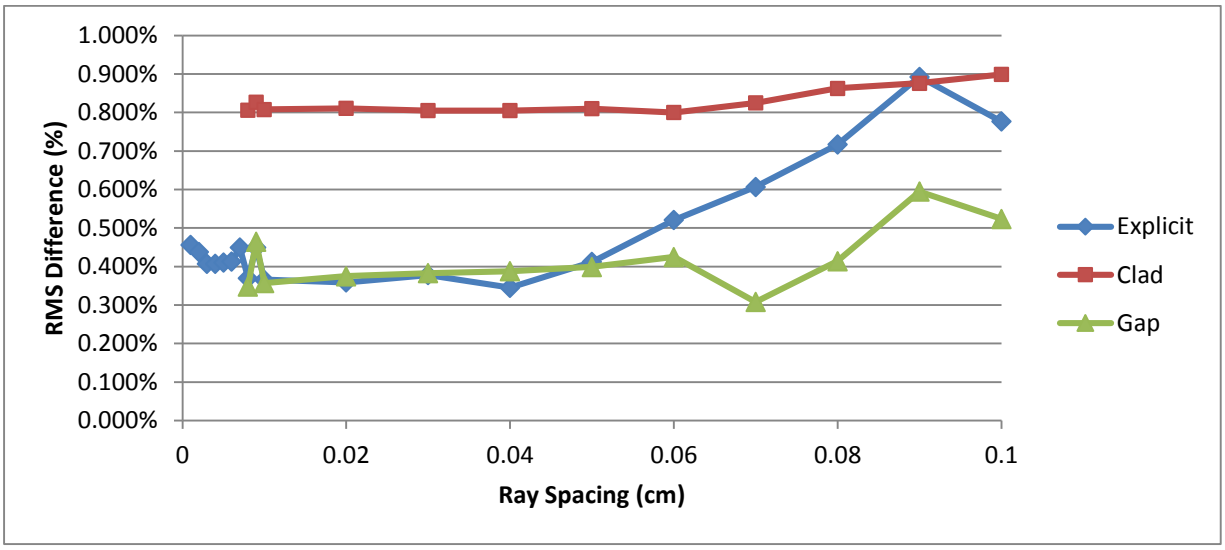

Figure 25. Pin power RMS differences of AP1000 Full Core 2D Plane with smeared IFBA regions at various ray spacings compared to CE-KENO

Volume weighting the IFBA material into the clad gives worse k-eff and pin powers than explicitly modeling the thin layer for any given ray spacing. Smearing into the clad does reduce the dependence on ray spacing because the clad is a larger region, but the volume smearing leads to inaccurate results. This could be addressed through the use of a flux weighted homogenization, but would require an additional level of calculations. When smeared into the gap, Figure 24 shows that the k-eff difference follows closely with the curve of the explicitly modeled cases. Therefore, smearing into the gap picks up the general effect of the IFBA layer. When Figure 25 and Figure 26 are examined, the pin powers generally follow closely with the explicitly modeled curves for finer ray spacings. As a result, volume weighting and

homogeneously smearing the IFBA material into the gap captures the general effect of the IFBA region, but one must run at a sufficiently fine ray spacing such that there is no advantage gained in terms of computation time.

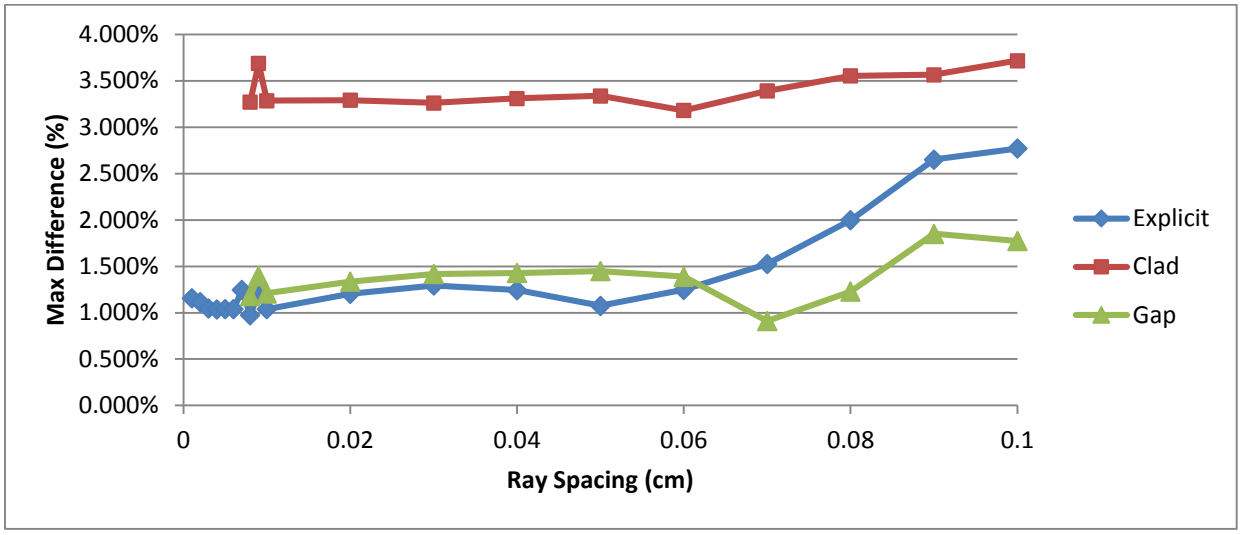

Figure 26. Maximum pin power differences of AP1000 Full Core 2D Plane with smeared IFBA regions at various ray spacings compared to CE-KENO

3.6 Non-Volume Weighted Segment Lengths

As discussed in Section 1.4.4, the segment length $s_{i,m,k}$ is renormalized to ensure an exact numerical integration of the discrete region volume. However, because the IFBA region is so small, there is a concern that the fraction in Equation (23), also known as a volume weighting factor, could become extremely large due to round off error. To evaluate this concern, the volume weighting factors generated when running the single IFBA pin cell, described in Section 2.1, were saved and are graphed in Figure 27. As seen from this semi log plot, most of the volume weighting factors are very close to unity. However, there are a few outliers that are as far away as three times and a third the original segment length. There were also eight "Infinity" factors calculated, which are shown in the last column in Figure 27.

These factors that appear far from unity raise concerns, so the same process was performed again, but this time saving all of the volume weighting factors generated when running a full core AP1000 model, as described in Section 2.3. These factors are graphed in Figure 28. With many more factors computed for this larger problem, they got as large as 152, and also included 74 "Infinity" factors.

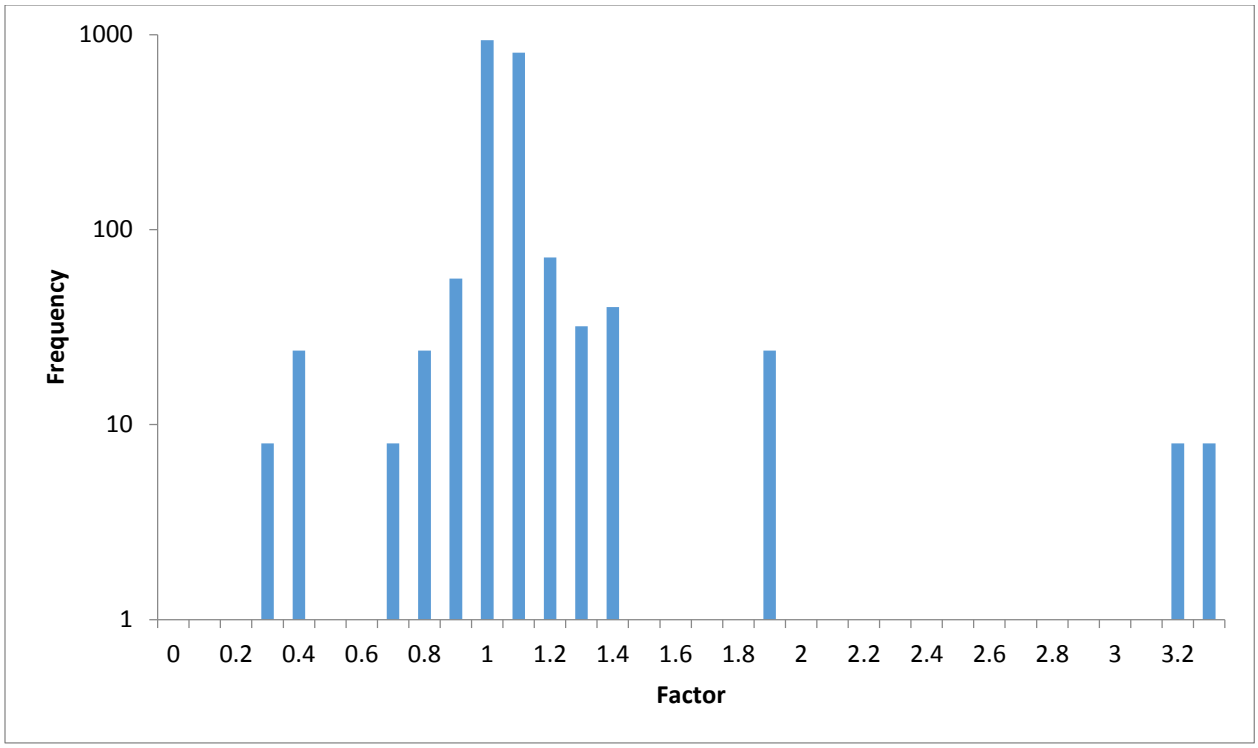

Figure 27. Segment length volume weighting factors for 2D single pin cell

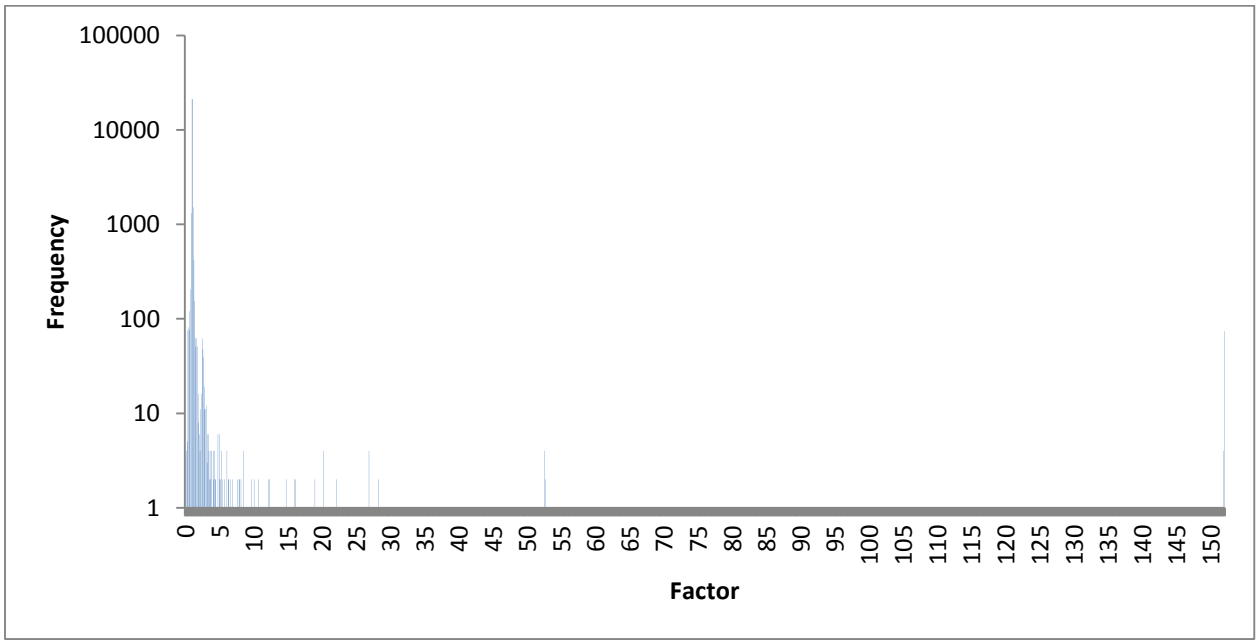

Figure 28. Segment length volume weighting factors for full core AP1000 2D midplane

To test the effect of volume weighting the segment lengths in IFBA problems, the single 2D pin cell was rerun, but with the volume weighting factor fixed to unity. The eigenvalue was compared to the CE-KENO benchmark and the difference was plotted along with those from the volume weighted case in Figure 29. It is clear that, by not volume weighting the segment lengths in the 2D pin cell case, the eigenvalue is very sporadic and not well-behaved. It required fine ray spacings for the non-weighted curve to settle down.

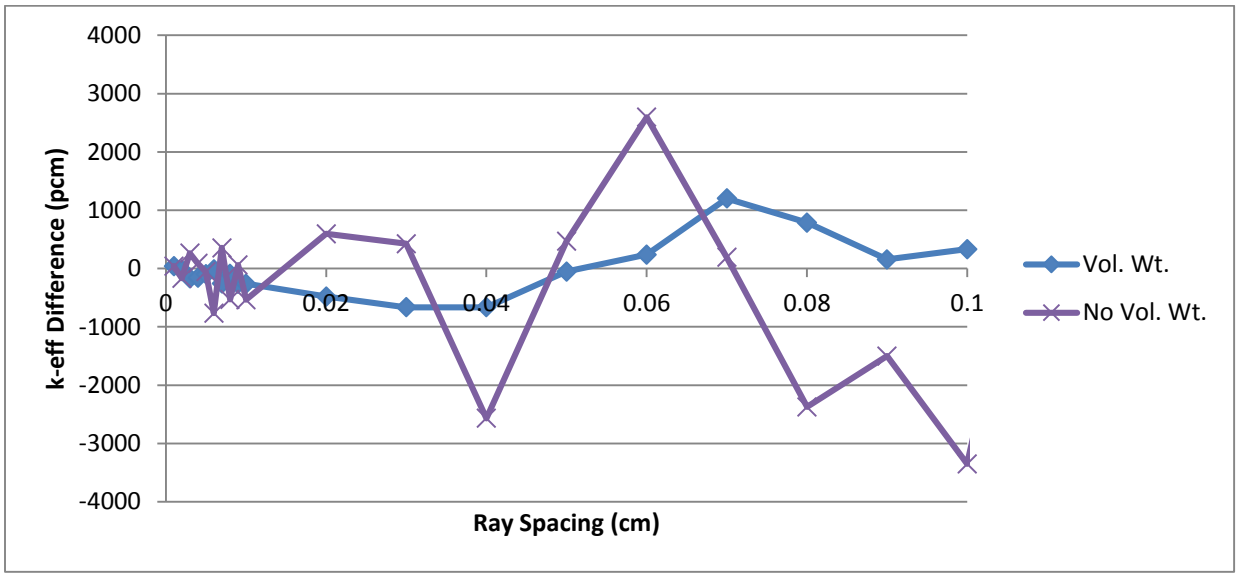

Figure 29. Eigenvalue differences for 2D pin cell compared to CE-KENO for both volume weighting and not volume weighting cases

In addition to the 2D pin cell case, the AP1000 2D midplane case was also rerun with the volume weighting factors set to unity. The eigenvalue differences for these cases are shown in Figure 30. For this full core case, the eigenvalue trend is much more stable for the not volume weighting case and, in fact, is more accurate for the standard ray spacing of 0.05 cm and finer. This could possibly be the result of cancellation of other errors introduced in the code, and not necessarily indicative of a more accurate method.

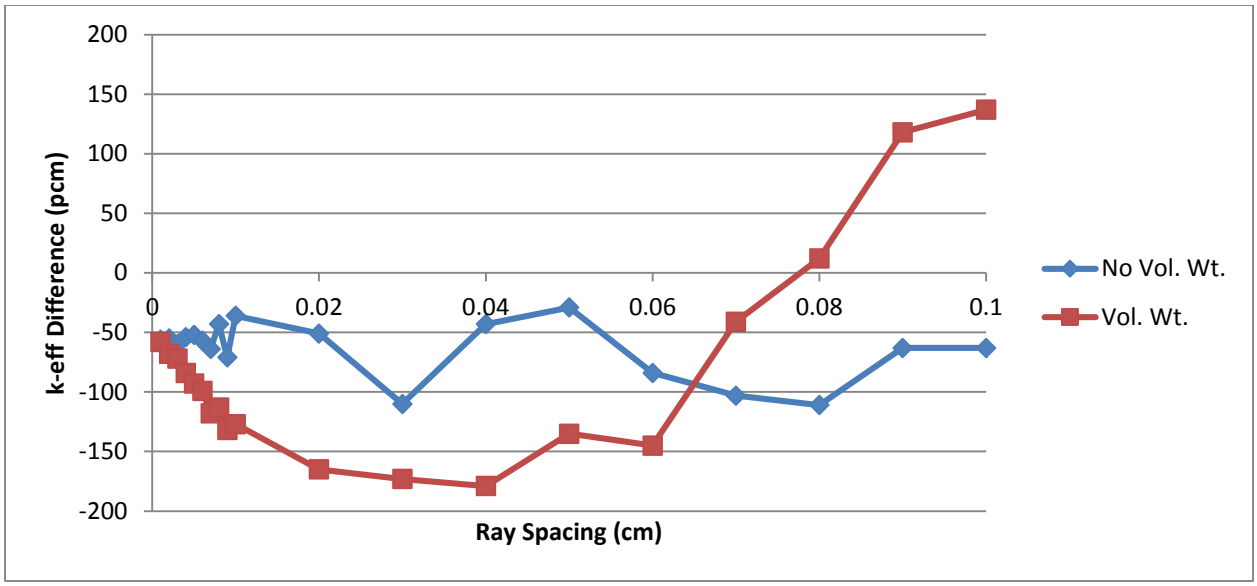

Figure 30. Eigenvalue differences for full core AP1000 2D midplane compared to CE-KENO for both volume weighting and not volume weighting cases

The RMS and maximum pin power differences with respect to CE-KENO are shown in Figure 31 and Figure 32, respectively. While the eigenvalue is stable and more accurate for the not volume weighting case, the RMS and maximum pin powers appear to be unstable and in most cases, is less accurate than the volume weighting cases. Therefore it appears that volume weighting is in fact the proper course of action for capturing the effect of IFBA, not only on the eigenvalue, but on the local pin power distribution.

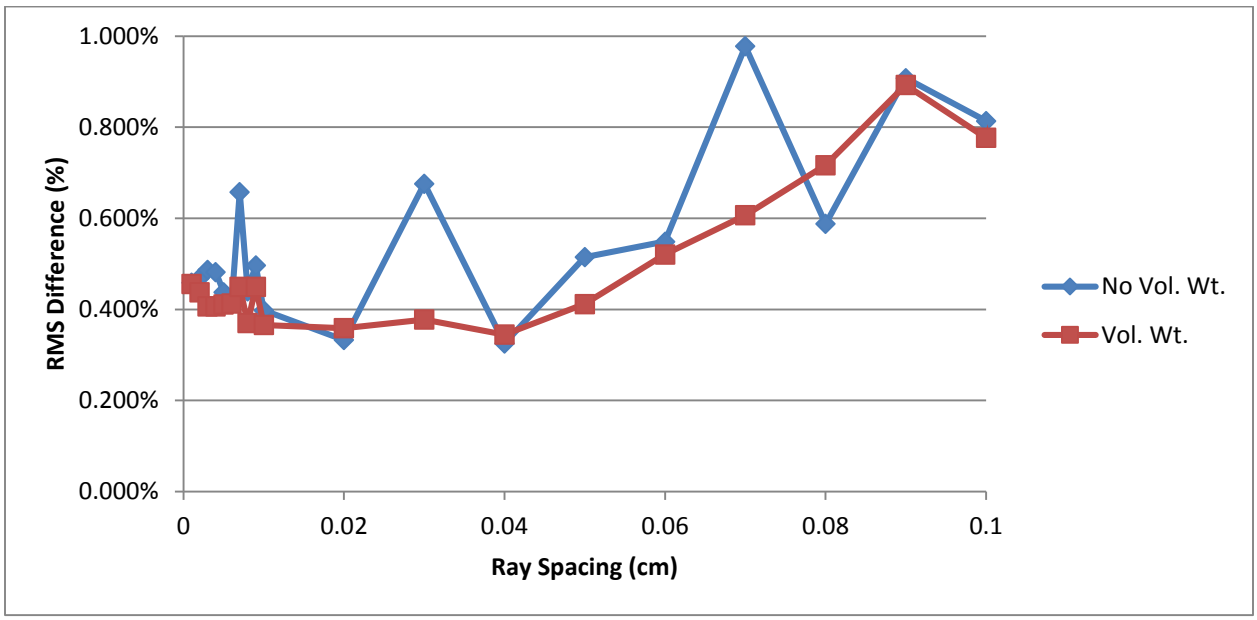

Figure 31. RMS pin power differences for full core AP1000 2D midplane compared to CE-KENO for both volume weighting and not volume weighting cases

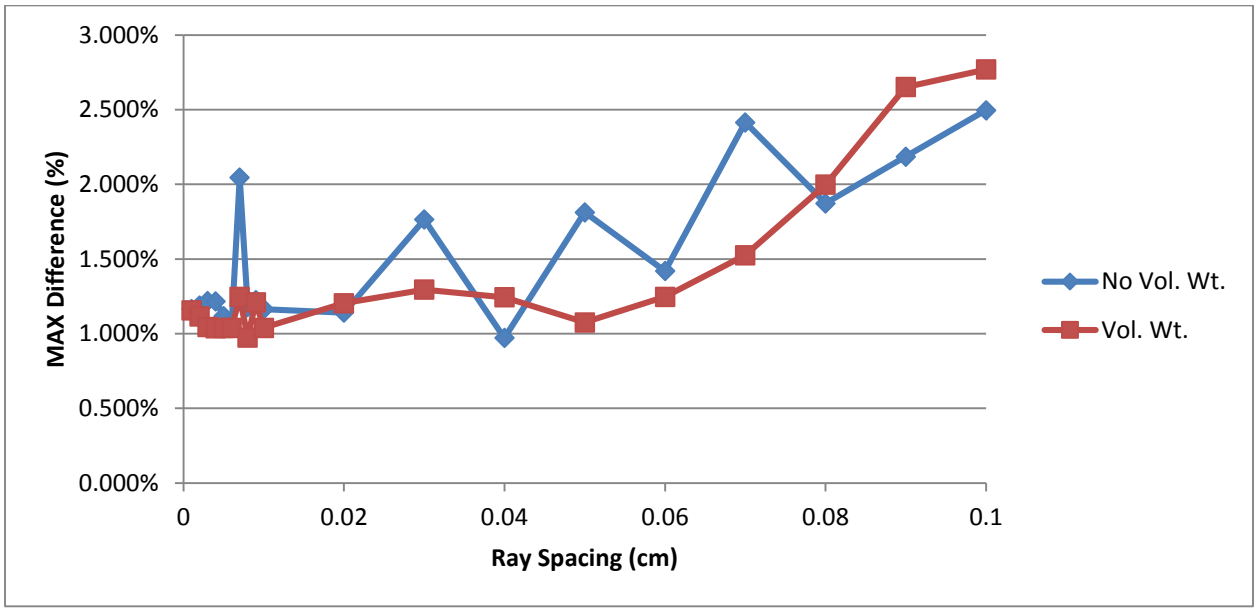

Figure 32. Maximum pin power differences for full core AP1000 2D midplane compared to CE-KENO for both volume weighting and not volume weighting cases

3.7 Depletion

A sensitivity study was conducted in order to determine the ray spacing needed to capture the effects of IFBA throughout the life of the fuel. A benchmark case was run with a ray spacing of 0.0005 cm which is the approximate thickness of the IFBA layer in the AP1000 full core 2D plane model. This benchmark case was also run with four times as many depletion steps as a standard depletion calculation. This case is considered the reference for comparing results. For all of the depletion cases run, a critical boron search was performed. The differences in boron concentration for various ray spacings when compared to this benchmark are shown in Figure 33.

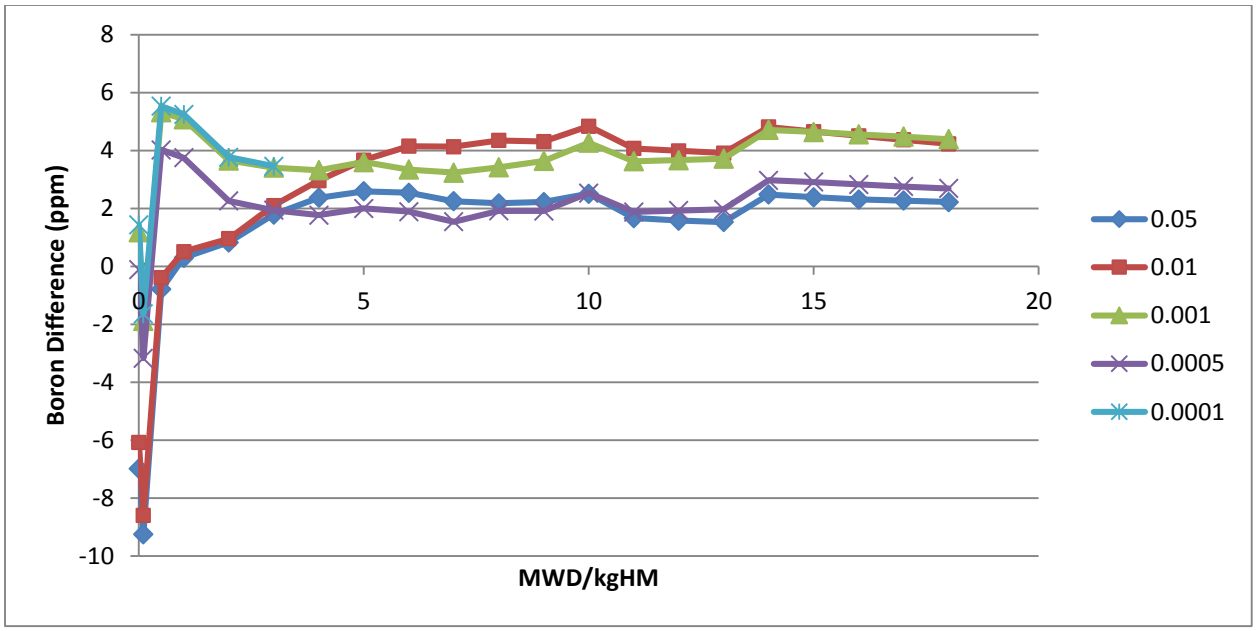

Figure 33. Boron concentration differences of AP1000 Full Core 2D Plane at various ray spacings compared to benchmark case

While the standard ray spacing of 0.05 cm gives the worst results for the first two time steps, this difference is still within 10 ppm. Using the rule of thumb that 1ppm ≈ 10 pcm, this difference is less than 100 pcm. After these first few time steps, the boron concentration differences converge and begin to flatten out.

Next the effect of time step size was analyzed and compared to the benchmark calculation. A ray spacing size of 0.001 cm was chosen as a more accurate ray spacing than the standard, while also being more feasible to run in terms of computation time. The 0.001 cm case from Figure 33 was rerun with twice as many substeps, twice as many timesteps, and four times as many timesteps. These results are displayed in Figure 34. The 0.001 cm case with the standard stepping is the worst case for the first few time steps, but is only off from the benchmark by less than 5 ppm. The case with twice as many substeps and the case with twice as many timesteps follow the same trend and eventually flatten out. The case running four times as many timesteps remains constant throughout the depletion and differs by about 1 ppm from the benchmark case. While it appears that four times as many timesteps are needed in order to differ from the benchmark by a constant value, the standard stepping differs from the benchmark by a maximum of less than 5 ppm and therefore should be sufficient for depletion calculations.

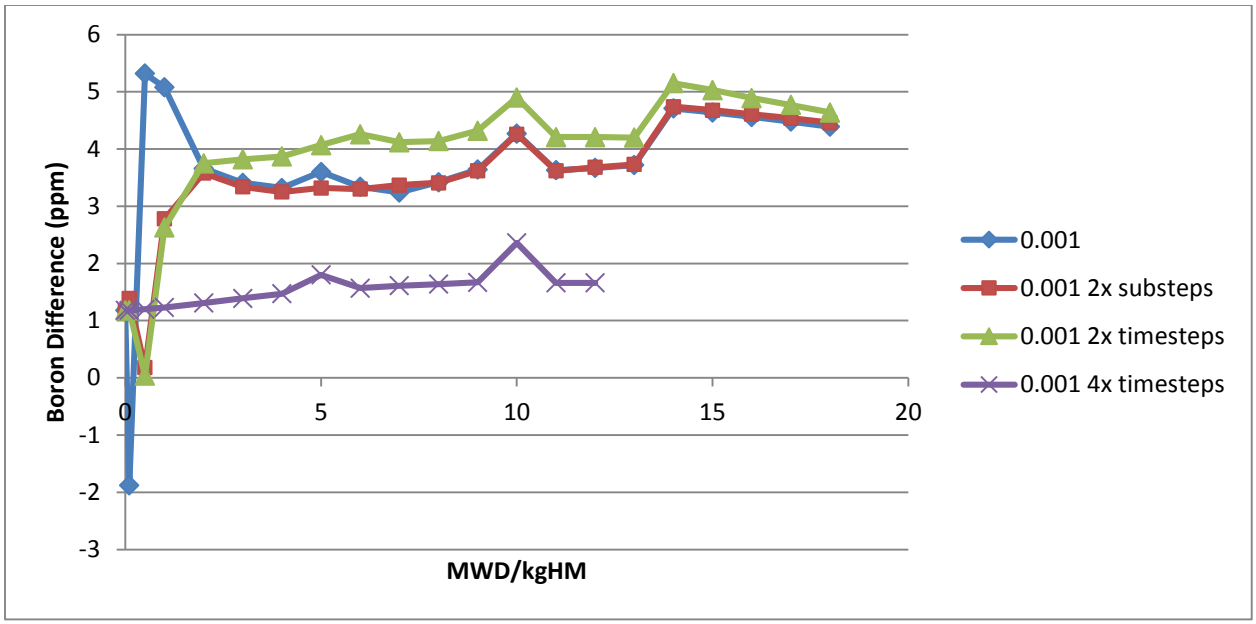

Figure 34. Boron concentration differences of AP1000 Full Core 2D Plane with different step sizes compared to benchmark case

3.8 Run Time

A major concern with refining the ray spacing in order to increase accuracy for full core problems is the increase in run time. Table 6 below summarizes the number of cores used for each depletion case as well as its run time. All of the cases were run on the Oak Ridge Leadership Computing Facility machine Eos with hyper threading. On Eos, each compute node contains two 8-core nodes, for a total of 16 cores. Each of these physical cores can function as two logical cores if hyper threading is enabled. These "virtual" cores are included in the Cores tally in Table 6. The 0.0005 cm benchmark case was able to exceed the 24 hour wall time on Eos by using restart files in order to span the depletion over three separate jobs.

Table 6: Summary of run times for all depletion cases

Case	Cores	Run Time (hh:mm:ss)
0.05	3008	5:18:43
0.01	3008	7:35:04
0.001	3536	8:56:12
0.0005	3536	16:38:52
0.0001*	3536	24:00:00
0.001 2x substeps	3536	9:09:09
0.001 2x timesteps	3536	16:46:41
0.001 4x timesteps†	3536	24:00:00
0.0005 Benchmark	3536	67:13:10

* Only completed first six time steps before hitting the wall time
† Only completed first fifteen time steps before hitting the wall time

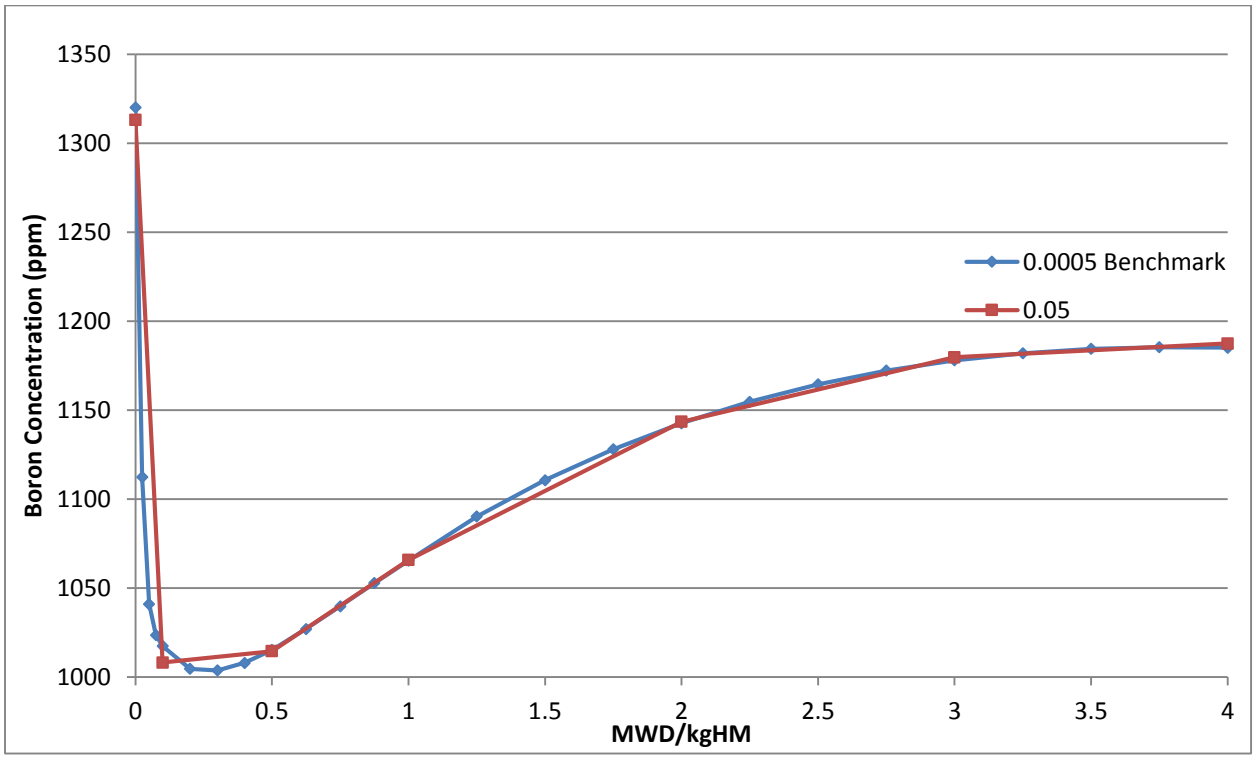

Figure 35. Comparison of boron concentrations between the benchmark and standard cases

Therefore, when comparing both the accuracy of each case and the run times required to complete them, it becomes apparent that the additional improvement in accuracy is not worth the increase in run time. The benchmark case ran 12.7 times longer, on 528 more cores, than the default 0.05 cm ray spacing with standard step sizes for a maximum gain in accuracy of only 8.6 ppm. Figure 35 shows the boron concentrations of both the benchmark case and the standard case for the first four MWD/kgHM, which is when the largest discrepancy occurs. If desired, few additional time steps could be run during this initial rapid change in soluble boron concentration in order to minimize error.

4. Conclusions

The accuracy of modeling IFBA using MOC at various ray spacings was examined for various problems. For the 2D single IFBA pin cell case, there is a strong dependence on ray spacing for accurate results. A ray spacing close to the thickness of the IFBA layer must be used in order to accurately capture its effects. A similar trend was seen when modeling a single 2D assembly containing IFBA, but the effect was lessened. However, for the AP1000 full core 2D midplane, the effect of ray spacing on accuracy was much less drastic. The thickness of the AP1000 IFBA layer is approximately 0.0005 cm, but the default ray spacing of 0.05 cm differed from the CE-KENO reference solution by only 135 pcm. An extreme case was run in which every other assembly in the AP1000 2D core slice was made entirely out of IFBA rods. The increased number of IFBA rods in the core led to a minor increase in the inaccuracy of the default ray spacing, causing the difference to rise to 153 pcm. Smearing the IFBA material into both the clad and gap were investigated as possible alternatives to modeling the IFBA layer explicitly. While volume weighting the IFBA into the clad always led to poorer results, smearing it into the gap seemed to capture most of its effect on the eigenvalue and pin powers. However, sufficiently fine ray spacings on the order of the default ray spacing are needed, so there is no advantage to doing so. The effect of ray spacing on the AP1000 2D core was investigated throughout depletion as well. While more accurate results can be gained through refining both the ray spacing and the time step size, these minor improvements in accuracy come at a huge cost of computation time. The soluble boron concentration result using the 0.05 cm default ray spacing with standard step sizes differed from a benchmark case by a maximum of only 8.6 ppm, while the benchmark case took 12.7 times longer to run on 528 more cores. Therefore it is suggested that for full core reactor design work, the method of characteristics is sufficient in modeling IFBA without any special treatment. However, for lattice and pin cell calculations, a means to resolve the IFBA modeling issue is needed. A recommendation for future work would be to implement a method such as the macro-band approach, group dependent angular quadrature, or flux weighted homogenization for these smaller scale problems.

References

[1] EIA, "Annual Energy Outlook 2014 with projections to 2040," DOE/EIA-0383(2014), 2014.

[2] U.S. NRC, "Power Reactors," 13 December 2013. [Online]. Available: http://www.nrc.gov/reactors/power.html. [Accessed October 2014].

[3] J. Askew, "A Characteristics Formulation of the Neutron Transport Equation in Complicated Geometries," AEEW-R-1108, 1972.

[4] D. Knott and A. Yamamoto, Handbook of Nuclear Engineering Vol. 2 - Lattice Physics Computations, ISBN: 978-0-387-98130-7: Springer, 2010.

[5] S. Pramuditya and M. Takahashi, "Core Design Study for Power Uprating of Integral Primary Systerm PWR," *Annals of Nuclear Energy*, vol. 59, pp. 16-24, 2013.

[6] K. Okumura, T. Kugo, K. Kaneko and K. Tsuchihashi, "SRAC2006: A Comprehensive Neutronics Calculation Code System," JAEA-Data/Code 2007-004, 2007.

[7] D. Pevec, D. Grgic and R. Jecmenica, "Core Design Calculations of IRIS Reactor Using Modified CORD-2 Code Package," in *Proceedings of the International Conference Nuclear Energy for New Europe 2002*, Kranjska Gora, 2002.

[8] D. Pevec, D. Grgic and R. Jecmenica, "FA2D Prediction Capability for NPP Kriska Fuel Assembly Calculation," in *Proceedings of the International Conference Nuclear Energy for New Europe 2008*, Portoroz, 2008.

[9] A. Trkov, "CORD-2 Package Users' Guide," IJS-DP-6948, 2009.

[10] G. Kristijan and D. Pevec, "Depletion Modeling of Integral Fuel Burnable Absorbers Containing Enriched Boron," in *5th International Conference on Nuclear Option in Countries with Small and Medium Electricity Grids*, Dubrovnik, 2004.

[11] M. Rosa, J. Warsa, J. Chang and R. Baker, "Discrete Ordinate Calculation of the k-Eigenvalue of an IFBA Pin Using Unstructured Meshes in 2D," in *Transactions of the American Nuclear Society*, Chicago, 2012.

[12] MPACT Development Team, "MPACT Theory Manual," University of Michigan, Ann Arbor, 2014.

[13] A. Godfrey, "VERA Core Physics Benchmark Progression Problem Specifications," Oak Ridge National Laboratory, CASL-U-2012-0131-004, 2013.

[14] F. Franceschini, A. Godfrey, J. Kulezsa and R. Oelrich, "Westinghouse VERA Test Stand - Zero Power Physics Test Simulations for the AP1000 PWR," Westinghouse, CASL-U-2014-0012-001, 2014.

[15] D. Hollenbach, L. Petrie and N. Landers, "SCALE: A Modular Code System for Performing Standardized Computer Analysis for Licensing Evaluation Vol. 2 - KENO-VI: A General Quadratic Version of the KENO Program," NUREG/CR-0200, Rev. 7, 2004.

Appendices

Appendix A – 2D IFBA Pin Cell VERA Input

```
[CASEID]
  title 'CASL AMA Benchmark Problem 1E - IFBA PIN - Public'

[STATE]
  power 0.0                       ! %
  tinlet 620.33 F                 ! F - 600K
  tfuel 600 K                    ! K
  modden 0.743                    ! g/cc
  boron 1300                      ! ppm

[CORE]
  size 1
  apitch 1.26
  height 1.0
  rated 0.01 0.01

  core_shape
    1

  assm_map
   IFBA

  bc_rad reflecting
  bc_top reflecting
  bc_bot reflecting

[ASSEMBLY]
  title 'ifba pin'
  npin 1
  ppitch 1.26

  fuel U31 10.257 94.5 / 3.1
  mat he 0.000176
  mat zirc 6.56 zirc4

  mat b10 1.0 b-10
  mat b11 1.0 b-11
  mat zr  1.0 zr
  mat ifba 3.85   zr 0.81306 b10 0.09347 b11 0.09347

  cell 1 0.4096 0.4106 0.418 0.475 / U31 ifba he zirc

  lattice LAT
    1

  axial IFBA  0.0 LAT 1.0

[EDITS]

[MPACT]
```

```
  vis_edits         core
  ray_spacing       0.05
!quad_set
  quad_type         CHEBYSHEV-YAMAMOTO
  polars_octant     2
  azimuthals_octant 16
!iteration_control
  flux_tolerance    1e-6
  num_inners        2
  k_tolerance       1e-6
  up_scatter        2
  num_outers        500
!cmfd
  cmfd              cmfd
  cmfd_solver       mgnode
  k_shift      1.5
  cmfd_num_outers   20
!parallel
  num_space         1
  num_angle         1
  num_energy        1
  num_threads         16
!xs_library
  xs_filename       declib56g_e7_09042013_p0mixed.fmt
  xs_type      ORNL
  subgroup_set      4
!mesh

  mesh fuel         3 1 1 / 8 8 8 8 8 8
  mesh gtube        3 1      / 8 8 8 8 8

  axial_mesh        1.0000
```

Appendix B – 2D IFBA Lattice VERA Input

```
[CASEID]
  title 'CASL AMA Benchmark Problem 2M - Fuel Lattice - Public'

[STATE]
  power 0.0                       ! %
  tinlet 620.33 F                 ! F - 600K
  tfuel 600 K                     ! K
  modden 0.743                    ! g/cc
  boron 1300                      ! ppm
  rodbank A 1                     ! rod fully withdrawn
  sym qtr

[CORE]
  size 1
  apitch 21.50
  height 1.0
  rated 0.01 0.01

  core_shape
    1

  assm_map
   128IFBA

  insert_map
    -

  crd_map
    AIC

  crd_bank
    A

  det_map
    -

  bc_rad reflecting
  bc_top reflecting
  bc_bot reflecting

[ASSEMBLY]
  title 'ifba assemblies'
  npin 17
  ppitch 1.26

  fuel U31 10.257 94.5 / 3.1
  mat he 0.000176
  mat zirc 6.56 zirc4
  mat b10 1.0 b-10
  mat b11 1.0 b-11
```

```
  mat zr  1.0 zr
  mat ifba 3.85 zr 0.81306 b10 0.09347 b11 0.09347

  cell 1 0.4096        0.418 0.475 / U31      he zirc
  cell X 0.4096 0.4106 0.418 0.475 / U31 ifba he zirc
  cell O          0.561 0.602 / mod zirc

  lattice LAT128
    O
    X 1
    X 1 1
    O X X O
    X 1 1 X 1
    X 1 1 X X O
    O X X O X X 1
    X 1 1 X 1 1 X 1
    1 X 1 1 X 1 1 1 X

  axial 128IFBA  0.0 LAT128 1.0

[EDITS]

[MPACT]
  vis_edits         core
  ray_spacing       0.05
!quad_set
  quad_type         CHEBYSHEV-YAMAMOTO
  polars_octant     2
  azimuthals_octant 16
!iteration_control
  flux_tolerance    1e-6
  num_inners        2
  k_tolerance       1e-6
  up_scatter        2
  num_outers        500
!cmfd
  cmfd              cmfd
  cmfd_solver       mgnode
  k_shift      1.5
  cmfd_num_outers   20
!parallel
  num_space         1
  num_angle         1
  num_energy        1
  num_threads       16
!xs_library
  xs_filename       declib56g_e7_09042013_p0mixed.fmt
  xs_type      ORNL
  subgroup_set      4
!mesh

  mesh fuel         3 1 1 / 8 8 8 8 8 8
```

```
mesh gtube         3 1      / 8 8 8 8 8

axial_mesh         1.0000
```

Appendix C – Full Core AP1000 2D Midplane Input

```
[CASEID]
  title 'AP1000 PWR: 2D Core'

[STATE]
  power 0.0                              ! %
  tinlet 557.33 F                        ! F
  tfuel 565.0 K                          ! K
  modden 0.7441292                       ! g/cc
  boron 1321

  sym qtr
  feedback off

  rodbank
   AO 1
   MA 1
   MB 1
   MC 1
   MD 1
   M1 1
   M2 1
   S1 1
   S2 1
   S3 1
   S4 1

[CORE]
  size 15                ! Assemblies across core
  apitch 21.50           ! All dimensions cm
  height 1.0             !
  rated 3400             ! MW

  baffle ss 0.127 2.54

  bc_top reflecting
  bc_bot reflecting

 core_shape ! 1=assembly, 0=nothing/reflector (depending on other parameters)
    0 0 0 0 0 0 1 1 1 0 0 0 0 0 0
    0 0 0 0 1 1 1 1 1 1 1 0 0 0 0
    0 0 0 1 1 1 1 1 1 1 1 1 0 0 0
    0 0 1 1 1 1 1 1 1 1 1 1 1 0 0
    0 1 1 1 1 1 1 1 1 1 1 1 1 1 0
    0 1 1 1 1 1 1 1 1 1 1 1 1 1 0
    1 1 1 1 1 1 1 1 1 1 1 1 1 1 1
    1 1 1 1 1 1 1 1 1 1 1 1 1 1 1
    1 1 1 1 1 1 1 1 1 1 1 1 1 1 1
    0 1 1 1 1 1 1 1 1 1 1 1 1 1 0
    0 1 1 1 1 1 1 1 1 1 1 1 1 1 0
    0 0 1 1 1 1 1 1 1 1 1 1 1 0 0
    0 0 0 1 1 1 1 1 1 1 1 1 0 0 0
    0 0 0 0 1 1 1 1 1 1 1 0 0 0 0
    0 0 0 0 0 0 1 1 1 0 0 0 0 0 0

  assm_map
```

```
    158E0I
    420E68I  158E0I
    158E0I   420E68I 158E0I
    420E68I  158E0I  420E68I  158E0I
    158E0I   420E68I 158E0I   480E124I 158E0I
    420E68I  158E0I  480E124I 320E0I   320E0I
    480E124I 480E88I 320E0I   074E0I
    320E0I   074E0I

  insert_map
    -
    12W -
    -   12W -
    12W -   12W -
    -   12W -   8W  -
    12W -   8W  - -
    -   4W  -  -
    -   -

  crd_map
    AIC
    -   AIC
    W   -   W
    -   AIC -   AIC
    AIC -   AIC -   W
    -   AIC -   AIC -
    W   -   AIC -
    -   -

  crd_bank
    AO
    -  S1
    MD -  MA
    -  S3 -  S1
    M1 -  AO -  MC
    -  S2 -  M2 -
    MB -  S4 -
    -  -

  mat zirlo    6.5
  mat zirc4    6.5
  mat he       0.0001786
  mat ifba     3.28 zrb2
  mat ss       7.8
  mat ssspring 1.5 ss
  mat aic      10.1
  mat tungsten 19.2
  mat inc      8.2
  mat waba     2.36
  mat al2o3    2.56

[ASSEMBLY]
  npin 17
  ppitch 1.26

  fuel U074   10.28 94.354 / 0.740   u-234=0.0056 u-236=0.00
  fuel U158   10.28 94.354 / 1.580   u-234=0.0130 u-236=0.0019
```

```
  fuel U158B  10.30 94.641 / 1.580   u-234=0.0130 u-236=0.0019
  fuel U320   10.28 94.354 / 3.200   u-234=0.0277 u-236=0.0006
  fuel U320B  10.30 94.641 / 3.200   u-234=0.0277 u-236=0.0006
  fuel U320AB 10.37 94.354 / 3.200   u-234=0.0277 u-236=0.0006
  fuel U340   10.28 94.354 / 3.400   u-234=0.0296 u-236=0.0008
  fuel U380   10.28 94.354 / 3.800   u-234=0.0347 u-236=0.0010
  fuel U400   10.28 94.354 / 4.000   u-234=0.0363 u-236=0.0010
  fuel U420   10.28 94.354 / 4.200   u-234=0.0388 u-236=0.0008
  fuel U440   10.28 94.354 / 4.400   u-234=0.0392 u-236=0.0029
  fuel U480   10.28 94.354 / 4.800   u-234=0.0449 u-236=0.0147

! IFBA OD is 0.41008
! Guide Tube and Instrument Tube
  cell 011                            0.56134  0.61214 /                  mod   zirlo
! Fuel, Region A
  cell 111          0.409575          0.41783  0.47498 /         U074     he    zirlo
! Fuel, Region B
  cell 211          0.409575          0.41783  0.47498 /         U158     he    zirlo
! Fuel, Region C
  cell 311          0.409575          0.41783  0.47498 /         U320     he    zirlo
! Fuel, Region D
  cell 411          0.409575          0.41783  0.47498 /         U340     he    zirlo
  cell 412          0.409575          0.41783  0.47498 /         U380     he    zirlo
  cell 413          0.409575          0.41783  0.47498 /         U420     he    zirlo
  cell 421          0.409575  0.410083 0.41783  0.47498 /  U340   ifba     he    zirlo
  cell 422          0.409575  0.410083 0.41783  0.47498 /  U380   ifba     he    zirlo
  cell 423          0.409575  0.410083 0.41783  0.47498 /  U420   ifba     he    zirlo
! Fuel, Region E
  cell 511          0.409575          0.41783  0.47498 /         U400     he    zirlo
  cell 512          0.409575          0.41783  0.47498 /         U440     he    zirlo
  cell 513          0.409575          0.41783  0.47498 /         U480     he    zirlo
  cell 521          0.409575  0.410083 0.41783  0.47498 /  U400   ifba     he    zirlo
  cell 522          0.409575  0.410083 0.41783  0.47498 /  U440   ifba     he    zirlo
  cell 523          0.409575  0.410083 0.41783  0.47498 /  U480   ifba     he    zirlo


! Fuel, Region A
  lattice TOPFUEL1
    011
    111 111
    111 111 111
    011 111 111 011
    111 111 111 111 111
    111 111 111 111 111 011
    011 111 111 011 111 111 111
    111 111 111 111 111 111 111 111
    111 111 111 111 111 111 111 111 111

! Fuel, Region B
  lattice TOPFUEL2
    011
    211 211
    211 211 211
    011 211 211 011
    211 211 211 211 211
    211 211 211 211 211 011
    011 211 211 011 211 211 211
    211 211 211 211 211 211 211 211
    211 211 211 211 211 211 211 211 211
```

```
! Fuel, Region C
  lattice TOPFUEL3
    011
    311 311
    311 311 311
    011 311 311 011
    311 311 311 311 311
    311 311 311 311 311 011
    011 311 311 011 311 311 311
    311 311 311 311 311 311 311 311
    311 311 311 311 311 311 311 311 311


! Fuel, Region D, 68 IFBA
  lattice TOPFUEL4
    011
    412 423
    412 413 423
    011 412 412 011
    412 413 423 412 412
    412 413 423 412 412 011
    011 412 412 011 412 412 412
    412 412 412 422 412 412 412 422
    421 411 421 411 421 411 421 411 421

! Fuel, Region E, 88 IFBA
  lattice TOPFUEL5
    011
    512 513
    512 513 513
    011 512 512 011
    512 513 523 512 512
    512 513 523 512 512 011
    011 512 512 011 512 512 512
    522 512 522 522 512 512 512 512
    521 521 521 521 521 521 511 521 511

! Fuel, Region E, 124 IFBA
  lattice TOPFUEL6
    011
    512 523
    512 513 513
    011 512 512 011
    512 513 523 512 512
    512 523 523 512 512 011
    011 512 512 011 522 512 512
    522 512 522 522 512 512 512 522
    521 521 521 521 521 521 521 521 521

  axial 074E0I    0.0 TOPFUEL1 1.0
  axial 158E0I    0.0 TOPFUEL2 1.0
  axial 320E0I    0.0 TOPFUEL3 1.0
  axial 420E68I   0.0 TOPFUEL4 1.0
  axial 480E88I   0.0 TOPFUEL5 1.0
  axial 480E124I  0.0 TOPFUEL6 1.0
```

```
[INSERT]
  title "WABA"
  npin 17
  cell 041  0.29 0.34 0.35 0.40386 0.41783 0.48387 / mod zirc4 he waba he
zirc4

  rodmap  4waba
    -
    -   -
    -   -   -
    -   -   -   -
    -   -   -   -   -
    -   -   -   -   -   041
    -   -   -   -   -   -   -
    -   -   -   -   -   -   -   -
    -   -   -   -   -   -   -   -   -


  rodmap  8waba
    -
    -   -
    -   -   -
    041 -   -   -
    -   -   -   -   -
    -   -   -   -   -   041
    -   -   -   -   -   -   -
    -   -   -   -   -   -   -   -
    -   -   -   -   -   -   -   -   -



 rodmap  12waba
    -
    -   -
    -   -   -
    041 -   -   -
    -   -   -   -   -
    -   -   -   -   -   041
    041 -   -   -   -   -   -
    -   -   -   -   -   -   -   -
    -   -   -   -   -   -   -   -   -



  axial   4W  0.0 4waba  1.0
  axial   8W  0.0 8waba  1.0
  axial  12W  0.0 12waba 1.0


 [CONTROL]
   !OMITTED

[DETECTOR]

[EDITS]
axial_edit_bounds
    0.0 1.0
```

```
[MPACT]
  jagged            true
  vis_edits         core
  ray_spacing       0.05
!quad_set
  quad_type         CHEBYSHEV-YAMAMOTO
  polars_octant     2
  azimuthals_octant 16
!iteration_control
  flux_tolerance    1e-6
  num_inners        2
  k_tolerance       1e-6
  up_scatter        2
  num_outers        500
  scattering        P2
!cmfd
  cmfd              cmfd
  cmfd_solver       mgnode
  k_shift           1.5
  cmfd_num_outers   20
!2D1D
  split_TL          true
  TL_treatment      lflat
  nodal_method      nem
! under_relax       1.0
!parallel
  num_space         47
  num_angle         1
  num_energy        1
  num_threads         16
  par_method        EXPLICITFILE
  par_file          part_3dcore_baffle_47r_64z.txt
!xs_library
  xs_filename       declib56g_e7_09042013_p0mixed.fmt
  xs_type           ORNL
  subgroup_set      4
!mesh
  mesh fuel         3 1 1 / 8 8 8 8 8 8
  mesh gtube        3 1   / 8 8 8 8 8
 !automesh_bounds   2 20 ! min, max
 !meshing_method    nonfuel
  axial_mesh        1.0
```

Vita

Erik Daniel Walker was born December 15, 1989 in Fort Smith, Arkansas to Richard and Sharon Walker. He is the youngest of three children: Jacqueline and Lauren. Erik attended Farmington High School in Farmington, Michigan. After graduating in 2008, he went on to study Nuclear Engineering and Radiological Science at the University of Michigan. While studying at Michigan, Erik worked as a research assistant in the field of radiation detection and measurement. He graduated in 2012 with a Bachelor of Science Degree.

After graduating, Erik worked as an intern for a summer at Knolls Atomic Power Laboratory in the Advanced Reactors Program. He then accepted a fellowship to the University of Tennessee through the Bredesen Center for Interdisciplinary Research and Graduate Education. Erik currently works as a graduate research assistant at Oak Ridge National Laboratory on the Consortium for Advanced Simulation of Light Water Reactors. He will obtain his Masters Degree in December of 2014 and will continue research towards his Ph.D. Eventually, Erik would like to pursue a career involving research and eventually teaching as a professor.

CASL-U-2015-0015-000